Centriolar satellites are dynamic membrane-less organelles that assemble via a hierarchical pathway

Efe Begar[1], Ece Seyrek[1], Selin Yilmaz[1], Melis D. Arslanhan[1], Ezgi Odabasi[1], Elif Nur Firat-Karalar[1,2]

[1]Department of Molecular Biology and Genetics, Koç University, Istanbul, Turkey 34450

[2]School of Medicine, Koç University, Istanbul, Turkey 34450

Corresponding Author:

Elif Nur Firat-Karalar

Department of Molecular Biology and Genetics

Koç University

Tel: (212) 3381677

E-mail: ekaralar@ku.edu.tr

Keywords: centriolar satellites, PCM1, centrosome, primary cilium, cilia, ciliopathies, microtubules, membrane-less organelle

Abstract

Centriolar satellites (CS) are ubiquitous, membrane-less organelles recognized for their dynamic organelle crosstalk, plasticity, diverse functions and links to developmental and neuronal diseases. Despite their significance, the mechanisms underlying CS assembly and homeostasis are unknown. Here, we developed *in vitro* and cellular CS biogenesis assays to spatiotemporally quantify the homeostatic properties of CS granules during assembly and maintenance. These assays revealed that CS assemble via a hierarchical pathway initiated by PCM1 scaffold formation followed by sequential recruitment of CS proteins. We discovered that PCM1 inherently forms granules through multimerization and phase separation, processes regulated by cytoskeleton and ciliopathy proteins. Additionally, PCM1 scaffold and clients are organized into subdomains within CS granules with distinct composition and dynamics. Selectively disrupting CS granule properties impaired the ciliary signaling functions of CS. Collectively, our results provide comprehensive insight into CS biogenesis and establish a conceptual framework and new tools to investigate context-dependent CS functions and their deregulation in disease. The mechanisms identified for CS may also explain the specificity and plasticity of other membrane-less organelles.

Introduction

The dynamic organization of the cytoplasm by partitioning molecules into membrane-less organelles, or biomolecular condensates, is an emerging mechanism for spatiotemporal control of cellular functions essential for development and physiology [1-4]. Most of these organelles such as stress granules, P bodies and germ granules form through multivalent interactions of scaffolding proteins via self-assembly, multimerization and phase separation of scaffolding proteins, which then concentrate or sequester specific macromolecules relevant to functions [5, 6]. Lack of a membrane enables them to rapidly assemble, disassemble and remodel in response to intrinsic and extrinsic stimuli, allowing cells to sense and adapt to changes in their environment. However, it also poses challenges in regulating size, composition and dynamics, and consequently, function.

Centriolar satellites (CS) are membrane-less organelles marked by their scaffolding protein Pericentriolar Material-1 (PCM1), which is essential for their assembly [7-11]. They were first discovered in epithelial cells as ~100 nm granules that cluster and move around the centrosomes in a microtubule-dependent manner [9]. In these cells, PCM1 interacts with over 200 proteins, collectively referred to as clients, some of which are mutated in developmental and neurodegenerative disorders [12-15]. They have since been recognized as part of a membrane-less trafficking pathway that stores, modifies and transports proteins to cellular structures such as centrosomes, cilia and autophagosomes [8, 10-12, 16, 17]. These activities play important roles in diverse cellular processes, many of which depend on this organelle crosstalk, and require highly dynamic and adaptive behavior [7, 18-20]. Among these processes are cell signaling (e.g. Hedgehog), cell division, motility, stress response, proteostasis and neurogenesis, as revealed by loss-of function studies in cells and animal models [7, 8, 10-12, 21-27]. Notably, PCM1$^{-/-}$ mice exhibit developmental defects and psychomotor and cognitive abnormalities, mirroring those observed in ciliopathies and schizophrenia [8, 23, 28]. These findings highlight the critical role of CS in development and differentiation.

CS are ubiquitous organelles that all contain PCM1, yet their homeostatic properties vary across different cell types and states [7, 18, 19, 29]. In multiciliated epithelial cells, CS appear as granules ranging from 1-6 µm, while in myotubes, they form a

matrix surrounding the nuclear envelope, and in oocytes, they are part of a liquid-like spindle domain [27, 30-32]. Moreover, CS properties adapt dynamically in response to diverse stimuli. For example, they disassemble during mitosis and reassemble upon mitotic exit. Their composition and size change during primary cilium assembly and under cellular stress [26, 33-35]. Additionally, individual CS granules within the same cell differ in size and composition [13, 36]. This observed intercellular and intracellular heterogeneity of CS highlight their highly plastic and adaptive nature.

Despite their significance, the mechanisms underlying their assembly and homeostasis are still poorly understood [7, 18-20]. Specifically, how PCM1 and clients form functional CS granules with the proper size, number, architecture and biochemical properties remain unknown. Cellular characterization of PCM1 so far has provided preliminary insights into assembly of the CS scaffold. The N-terminal half of PCM1, which contains two self-association domains, forms granules in cells, whereas the C-terminal half does not [29]. This suggests that multimerization might be sufficient for CS granule assembly. Additionally, the fusion and splitting behavior of CS granules in cells, their dissolution during mitosis with other phase-separated organelles and the high enrichment of intrinsically disordered regions (IDRs) in PCM1 indicates that phase separation plays a role in their assembly [27, 29, 37, 38]. Testing these and dissecting CS assembly requires tools for step-by-step monitoring of granule formation from its molecular components with high spatiotemporal resolution. This has been challenging because CS are constitutively present in cells, except during mitosis, unlike inducible organelles such as stress granules. Additionally, their small size limits the visualization of their assembly stages and kinetics using traditional imaging techniques.

To overcome these challenges, we developed *in vitro* and cellular CS biogenesis assays that allow for spatiotemporal analysis of the biophysical, compositional, morphological and dynamic properties of CS granules throughout their biogenesis and steady state. Using these assays, we discovered a hierarchical, multistep assembly pathway that leads to the formation of highly organized yet dynamic CS granules. These assays also enabled us to elucidate mechanisms underlying CS assembly and its homeostasis, revealing new regulators. Moreover, we leveraged this information to specifically disrupt CS properties and showed the functional significance of CS

homeostatic regulation in cellular signaling. Collectively, our findings introduce powerful new tools and establish a comprehensive framework for CS assembly. They also provide insights into the mechanisms behind CS heterogeneity and dynamics, which are essential for their spatiotemporal and context-dependent functions.

Results

CS granules are heterogeneous in their biophysical properties in cells

To elucidate the molecular mechanisms driving CS assembly, we first examined how disrupting key factors involved in the phase separation of membrane-less organelles affects the steady-state properties of CS [1, 5]. Specifically, we focused on multivalent interactions among RNAs, proteins, and RNA-protein complexes. These interactions are critical in defining the biophysical properties of condensates, which range from dynamic liquids to non-dynamic gel and solid states. Notably, RNA has recently been defined as a CS component [39]. To compare CS with a well-established RNA-dependent phase-separated organelle, we used stress granules as a positive control. To assess defects in CS integrity, we quantified both the total volume and the fluorescent intensity of PCM1 granules.

First, we examined the biophysical properties of PCM1 granules by assessing their sensitivity to 1,6-hexanediol (1,6-HD), which disrupts weak hydrophobic interactions and is used as a probe for liquid-like condensates. In human retinal pigment epithelial (RPE1) cells, 1,6-HD treatment reduced the total volume and intensity of PCM1 granules, indicating presence of a small liquid-like pool of CS (Fig. 1A, 1B). As a control, 1,6-HD treatment almost completely dissolved stress granules marked by G3BP1, which formed in cells upon treatment with sodium arsenite [40, 41]. Similar to wild-type cells, it dissolved only a fraction of PCM1 granules in sodium arsenite-treated cells (Fig. S1A, S1B). Notably, majority of PCM1 granules dissolved upon mitotic entry, concurrent with an increase in total PCM1 abundance, and reassembled upon exit in RPE1 cells, indicating rapid changes of their biophysical properties during cell division (Fig. S1C, S1D). Next, we tested the sensitivity of CS to RNase treatment and found that PCM1 granules remained resistant (Fig. 1A, 1B). As a control, RNase treatment

induced dissolution of stress granules in sodium arsenite-treated RPE1 cells (Fig. S1A, S1B).

Collectively, these results indicate that most PCM1 granules in interphase cells are solid-like, with a smaller fraction in a liquid-like state. Additionally, their structural integrity at steady state does not depend on RNA. These findings suggest a liquid-to-solid transition during CS assembly or alternatively CS granules are multiphase, with PCM1 occupying both liquid and solid subdomains.

In vitro **reconstitution reveals granule formation, client sequestration and microtubule affinity as inherent PCM1 properties**

An essential first step in elucidating CS assembly mechanisms is characterization of PCM1, as it is the only protein essential for this process. We hypothesized that self-assembly of PCM1 drives CS scaffold assembly via phase separation. This could be either intrinsically due to its molecular structure through homotypic interactions or dependent on cellular factors. To test this, we performed *in vitro* reconstitution experiments to assess the ability of recombinant PCM1 to form condensates. First, we expressed and purified His-MBP-mNeonGreen-PCM1 (referred to as mNG-PCM1) from insect cells, fixed and precipitated the purified protein on coverslips, and confirmed the presence of full-length PCM1 by staining with antibodies specific to its N- and C-terminal regions. Notably, the signals from these antibodies occupied distinct subdomains within the PCM1 structures (Fig. S1E, S1F). Immunoblotting staining further verified the purification (Fig. S1E). Mass spectrometry confirmed mNG-PCM1 as the most abundant protein and detected no known centrosome components or microtubule regulators, except for negligible amounts of DYNLL1 and DYNLL2 (both at 0.08%) (Fig. S1G, Table S1).

To screen for its phase separation ability, we assessed whether PCM1 forms condensates in buffers with varying protein or crowding reagent concentrations. First, we observed 1 μM PCM1 in a physiological low salt buffer containing 150 mM NaCl using fluorescence microscopy in a flow chamber (Fig. 1C). We chose this concentration to mimic the cellular environment, as its intracellular concentration is around 700 nM in U2OS and HEK293T cells and 900 nM in Jurkat cells [42-44]. After a

brief assembly period (less than 5 min), 1 μM mNG-PCM1 formed condensates with a mean diameter of 0.54 μm (Fig. 1C). Notably, the mNG signal, which tags PCM1 at its N-terminus, appeared as a spheroidal shape, which was resolvable in larger condensates, suggesting there is spatial organization (Fig. 1C inset). With increasing protein concentrations of 1, 2, 3, and 4 μM PCM1, the number of PCM1 condensates increased, yet their size remained mostly constant, suggesting size regulation of PCM1 granules (Fig. 1D, 1E). As a negative control, mNG alone did not form condensates at these concentrations (Fig. S1H). In the presence of a crowding agent (10% PEG), PCM1 primarily assembled into micron-scale scaffolds rather than individual condensates. The condensates adhered to each other instead of fusing and had non-spherical shapes, consistent with a solid-like state (Fig. S1I).

Consistent with biophysical properties of PCM1 granules in cells, assembly of recombinant PCM1 condensates was sensitive to 1,6-HD (Fig. 1F, 1G). Specifically, 1,6-HD dissolved smaller condensates and made the remaining ones adhere, thus increasing their average volume (Fig. 1F, 1G). Together, these results show that homotypic interactions among PCM1 molecules are sufficient to drive formation of predominantly solid-like condensates *in vitro* and explains how PCM1 acts as the structural scaffold for CS.

Finally, we investigated whether *in vitro* PCM1 condensates recapitulate cellular properties of CS granules. Given that CS associate with and move along microtubules, we first explored whether PCM1 condensates interact with microtubules. To this end, we performed TIRF analysis by introducing mNG-PCM1 condensates onto taxol-stabilized rhodamine microtubules crosslinked to the coverslip (Fig. 1H). In this reaction, mNG-PCM1 condensates interacted with microtubules, confirming that there is a direct interaction between them (Fig. 1H). Next, we assessed the ability of PCM1 condensates to selectively sequester clients. Given its importance in CS homeostasis and functions, we chose the ubiquitin ligase MIB1 as the candidate CS client to test *in vitro*. We purified His-MBP-mScarlet-MIB1 from bacteria and used 100 nM concentration in condensate assays, which reflects its cellular levels (Fig. S1J) [42-44]. When incubated separately in condensate buffer, both PCM1 and MIB1 formed condensates (Fig. 1I).

Upon adding MIB1 to pre-formed PCM1 condensates, MIB1 was rapidly recruited, resulting in the formation of co-condensates (Fig. 1I). As a selectivity control, PCM1 condensates did not sequester GST-mScarlet (Fig. 1I). These findings show that the PCM1 scaffold can selectively sequester MIB1 on its own, underscoring its essential role in determining the specific composition of CS granules in cells.

Cellular reconstitution defines PCM1 as a modular protein with domains essential for granule formation and regulation of granule properties

Given that *in vitro* reconstitution assays suggested homotypic PCM1 interactions drive CS scaffold assembly by phase separation, we further explored this using cellular reconstitution experiments. The human *PCM1* gene encodes a 2024 amino-acid (aa) acidic protein that is highly enriched in IDRs (Fig. 2A) [45]. Its N-terminal 1550 aa region contains eight coiled-coil domains and two self-association domains, while its C-terminal region includes the conserved PCM1-C domain and a LC3-interacting region (LIR) motif (Fig. 2A) [16, 29, 46-48]. To investigate how PCM1 scaffolds CS assembly through multimerization-based phase separation in cells, we designed PCM1 deletion mutants to include one or two self-association domains, or to exclude them. We then assessed their interactions, biophysical properties and ability to form granules in cells. Specifically, we used GFP-fusions of full length PCM1 (PCM1) along with deletion mutants PCM1-N (1-1200 aa), PCM1-NS (1-700 aa), PCM1-M (700-1200 aa) and PCM1-C (1200-2024 aa) (Fig. 2B).

We first performed cellular reconstitution experiments to identify the PCM1 regions required for granule assembly in Hela::PCM1 KO cells (Fig. 2C). GFP-PCM1 formed granules similar to those of endogenous PCM1, clustering around the centrosomes and distributing to a lesser extent throughout the cytoplasm (Fig. 2C). GFP-PCM1-N and GFP-PCM1-M also induced granule formation (Fig. 2C). However, these granules were much larger and more variable in size than those formed by PCM1. Importantly, despite having a self-association domain, GFP-PCM1-NS did not induce granule formation in these cells (Fig. 2C). Similarly, GFP-PCM1-C did not form granules (Fig. 2C). Solubility analysis further showed that PCM1-M and PCM1-N are

more insoluble compared to PCM1 and PCM1-C (Fig. 2D), likely due to their tendency to form larger, irregular granules.

To assess the impact of endogenous PCM1 on granule formation, we performed similar experiments in wild-type HeLa cells. All mutants showed consistent behavior except for PCM1-NS, which formed granules, potentially mediated by endogenous PCM1 (Fig. 2C). Supporting this, granules formed by PCM1-N, PCM1-M, and PCM1-NS in wild-type cells recruited endogenous PCM1, confirming their interaction at the CS granules (Fig. S2A). Taken together, these findings demonstrate that PCM1 is a modular protein with PCM1-M being the primary self-association region essential for CS granule formation. Meanwhile, PCM1-C influences CS properties such as size, number, and solubility, but is not necessary for assembly.

Finally, we assessed the phase separation propensities of PCM1 and deletion mutants by quantifying their critical saturation concentrations (Csat), the threshold at which phase separation begins. To quantify Csat, we exploited the variability in their expression levels in transiently-transfected PCM1 KO cells and measured relative protein granule and cytoplasmic concentrations through fluorescence intensity per volume after 3D reconstruction (Fig. 2E, 2F) [49]. We found that GFP-PCM1 remained formed granules when it reached its Csat and these granules dissolved when concentrations exceeded a certain threshold (Fig. 2E, 2F). This indicates tight control of CS size and number. In contrast, once the GFP-PCM1-N and GFP-PCM1-M granules formed, they did not dissolve at higher concentrations but instead became brighter and larger (Fig. 2E, 2F). Additionally, PCM1, PCM1-N, and PCM1-M behaved similarly in wild-type cells compared to PCM1 KO cells but showed lower Csat values, likely due to their self-association with endogenous PCM1 promoting granule formation at lower concentrations. (Fig. S2B, S2C).

Manipulation of PCM1 multimerization deregulates CS properties

Our characterization of PCM1 deletion mutants indicates that PCM1-C regulates PCM1-N's multimerization-based phase separation, highlighting the critical role of PCM1's modular organization in assembling CS granules with the appropriate size, number, and biophysical properties. This leads to the hypothesis that changing PCM1's

multimerization status could alter CS granule properties and lead to aberrant CS assembly and disassembly. To test this, we developed a tool for inducible manipulation of PCM1's multimerization state.

To control PCM1 multimerization in cells, we adapted the chemically inducible dimerization system using a modified FKBP protein (FKBP-F36V mutant) and its cell-permeable ligands: AP20187 for dimerization, known as the dimerizer, and AP22542 to reverse the process, referred to as the washout ligand (Fig. 2G) [50, 51]. FKBP12-F36V homodimerizes upon binding to the dimerizer, which can be rapidly (within several min) reversed with washout ligand. To adapt this system for CS, we designed a lentiviral expression construct for fusing mNG-PCM1 with FKBP-F36V at its C-terminus and generated RPE1::PCM1 KO cells stably expressing this chemically dimerizable PCM1 mutant (Fig. 2H). We then compared the number and size of CS granules in these cells before and after dimerization, and following dimer dissociation. Dimerizer treatment significantly reduced granule number and increased their size, which were reversed by washout ligand, confirming the role of regulated dimerization in controlling CS size and number (Fig. 2I). Live imaging of mNG-PCM1-FKBP after inducing dimerization or dissociation revealed the spatiotemporal dynamics of these changes in CS granule properties (Fig. S3A).

Given that CS integrity and biophysical properties are altered during cell division, we also examined how induced dimerization influences the mitotic behavior of CS granules (Fig. 2J, S3B). As expected, mNG-PCM1-FKBP dissolved during mitosis in untreated cells. However, in cells treated with dimerizer, mNG-PCM1-FKBP aggregates remained intact and were randomly distributed in the cytoplasm of mitotic cells (Fig. 2J). Notably, some cells displayed PCM1 aggregates in both daughter cells, while others had them in only one daughter cell (Fig. 2J). A similar pattern of mitotic behavior was observed by time-lapse imaging (Fig. S3B). These findings show that induced PCM1 dimerization prevents CS dissolution during mitosis and causes unequal CS distribution among daughter cells, highlighting the importance of regulated PCM1 multimerization in maintaining the biophysical properties of CS.

Given that inducible dimerization of PCM1 disrupts key CS properties, such as size and biophysical characteristics, this method provides a unique opportunity to

directly study the correlation between CS properties and their functions. This approach is advantageous as it does not involve eliminating PCM1, unlike previous studies that relied on depleting or deleting PCM1 for functional analysis. Therefore, we investigated whether altered CS granule properties via induced dimerization also affect CS function, specifically in cilium assembly and function. Ciliogenesis and cilium length were similar between control cells and those treated with dimerizer and washout ligand (Fig. S3C-E). However, cilia formed in the presence of dimerizer did not respond efficiently to the Hedgehog agonist SAG, as shown by a significant decrease in ciliary SMO concentration (Fig. 2K, 2L). Notably, this phenotype could be reversed by dissociating the mNG-PCM1-FKBP dimers with washout ligand (Fig. 2K, 2L). These results demonstrate that manipulating the multimerization of CS disrupts the formation of functional cilia and establishes a direct link between the regulation of CS properties and cellular signaling.

Development and validation of the *de novo* CS biogenesis assay

The mechanisms underlying CS assembly and its homeostatic regulation are not known. This gap in knowledge limits our ability to understand how CS heterogeneity is established and remodeled across various contexts to mediate their dynamic functions. To address this, we developed a *de novo* CS biogenesis assay that enables the spatiotemporal assessment of the biophysical, compositional, morphological, and dynamic properties of CS granules throughout their biogenesis. Our approach involved the inducible stable expression of GFP-tagged PCM1 and granule-forming deletion mutants, PCM1-N and PCM1-M, in RPE1::PCM1 KO cells. We did not include PCM1-C and PCM1-NS as their expression failed to reconstitute granule formation (Fig. 2C). To validate our approach, we first assessed whether PCM1 expression induces CS granule assembly by performing immunofluorescence analysis on cells stained with PCM1 antibodies after 16 h of induction. We observed the formation of PCM1, PCM1-N, and PCM1-M granules (Fig. S4A). To validate temporal expression of PCM1 in the stable lines, we immunoblotted them before induction and at 1, 2, 4, 8, and 16 h post-induction with PCM1. This analysis showed a gradual increase in PCM1 protein expression over time, starting as early as 1 h (Fig. S4B).

We next built a comprehensive temporal view of the global proteomic changes during *de novo* CS assembly. To this end, we used multiplexed tandem-mass tag (TMT)-based proteomic analysis of RPE1::PCM1 KO cells expressing GFP-PCM1 before induction and at 20 min, 1 h, 2 h, 16 h, and 48 h post-induction. We identified 6065 proteins with high confidence, 328 of which showed significant upregulation or downregulation across six time points (Fig. S4C). The time-dependent increase in PCM1 confirmed the inducible expression of PCM1 in our system (Fig. S4D). To identify proteins with expression profiles similar to or distinct from PCM1, we used hierarchical clustering to group differentially expressed proteins (hits) based on their expression patterns across different time points. The heatmap in Fig. S4D shows the expression profile of each hit protein and the clustering results. GO analysis of these clusters revealed significant enrichment of specific biological processes in clusters 1, 3, 6, and 8 (Fig. S4E). Cluster 6 and 8 contained PCM1 along with proteins that show increasing levels after dox induction (Fig. S4E). Notably, PCM1's expression profile closely aligned with proteins from compartments such as stress fibers, adherens junctions, focal adhesions, endoplasmic reticulum lumen, and exosomes (Fig. S4F). It also partially correlated with proteins from cluster 8, including those associated with the centrosome, chromosome, microtubule, kinesin complex, spindle, and nuclear lamina (Fig. S4F). Overall, the global proteome's reconfiguration upon PCM1 expression is consistent with the role of CS in proteostatic regulation and indicates potential new complexes involved in CS assembly.

To evaluate the physiological relevance of the *de novo* biogenesis assay, we examined the extent to which the *de novo* formed granules by GFP-tagged PCM1, PCM1-N and PCM1-M were functional. To this end, we performed phenotypic rescue experiments for CS-linked ciliary functions (Fig. S4G-M). Specifically, for the ciliary phenotypes, we examined efficient cilium assembly with correct length, proper targeting of the IFT-B machinery to the basal body and cilium, and activation of the Hedgehog pathway upon SAG treatment. Compared to wild-type cells, PCM1 KO cells exhibited a severe ciliogenesis defect (Fig. S4G, S4H). Cells expressing GFP-PCM1 efficiently formed cilia of comparable length and with IFT88 and SMO levels similar to those of control cells, demonstrating that these phenotypes are specific to PCM1 KO (Fig. S4G-

M). While GFP-PCM1-N fully rescued the ciliogenesis defect, it did not effectively restore the shorter cilium phenotype or the ciliary levels of IFT88 and SMO as well as PCM1, suggesting that the granules formed by PCM1-N are partially functional (Fig. S4G-M). In contrast, GFP-PCM1-M expression failed to rescue any of the assessed ciliary phenotypes, indicating that granule formation alone is not sufficient to rescue these defects (Fig. S4G-M). Taken together, our results show that GFP-PCM1 fully restored the defects reported in PCM1 knockout cells, validating our use of the *de novo* biogenesis assay to examine the assembly of functional CS granules. We used the lines expressing partially functional PCM1-N and dysfunctional PCM1-M granules for determining the contributions of different domains to CS biogenesis.

Spatiotemporal dynamics of PCM1 scaffold formation during CS biogenesis

CS can assemble either through random self-organization by stochastically recruiting its scaffold and clients from the cytoplasm, or via an ordered pathway where clients hierarchically assemble around the seeding scaffold. Given their highly regulated nature and our data showing PCM1's inherent ability to form granules *in vitro*, we hypothesized that CS granules assemble via a multistep process that begins with the formation of the PCM1 scaffold. To test this, we used CS biogenesis assays to define the spatiotemporal dynamics of PCM1 scaffold assembly, disassembly and reassembly. To quantify CS properties, we developed an analysis pipeline that measures the total and average volume or intensity of granules and their average distance from the centrosome (Fig. S5A).

Using the *de novo* CS biogenesis assay, we first performed fixed 3D confocal imaging to quantify the volume, fluorescence intensity and number and cellular positioning of assembling PCM1 granules at single-cell resolution before and after doxycycline (dox) induction (Fig. 3A, 3B, S5A, S5B). Cells were imaged at 10, 20, and 30 min, and 1, 2, 4, 8, and 16 h post-induction. Analysis of stable cells fixed and stained with the centriole marker centrin showed that GFP-PCM1, GFP-PCM1-N and GFP-PCM1-M initially formed at the centrosome (Fig. 3A, 3B). Subsequently, granules of various sizes formed in the cytoplasm and developed into characteristic pericentrosomal clusters over several hours, as indicated by the changes in the average distance of

granules from the centrosome (Fig. 3A, 3B). Notably, GFP-PCM1 granules were smaller and more uniform in size with a higher average number per cell, while GFP-PCM1-N and GFP-PCM1-M granules were larger and more heterogeneous in size (Fig. 3A, 3B).

To spatiotemporally describe different stages of PCM1 scaffold formation during CS biogenesis, we then performed time-lapse confocal imaging of GFP-PCM1, GFP-PCM1-N, and GFP-PCM1-M assembly dynamics. Using 3D constructed movies, we quantified CS granule properties, which were consistent with those observed in fixed imaging (Fig. 3C, 3D). Time-dependent analysis of PCM1 granule properties in individual cells revealed an early nucleation phase with the first granule forming at the centrosome within 10 to 30 min, followed by a growth phase from 30 min to 1-2 h where granule number, size, and intensity increased, and a late phase starting around 2 h when granule properties remained relatively stable (Fig. 3D, 3E). While PCM1-N and PCM1-M granules also underwent nucleation and growth phases, they did not reach the late steady phase (Fig. 3D, 3E). Instead, their size and fluorescence intensity continued to increase along with rising protein levels, while their number decreased, suggesting fusion events. For comparative analysis, we plotted granule volume against number, which more precisely revealed three distinct phases of CS biogenesis and highlighted the differences between PCM1 and its mutants (Fig. 3E). For example, PCM1 induced the formation of smaller but more granules, whereas PCM1-M and PCM1-N formed fewer, larger granules.

Next, we investigated the biophysical properties of the granules formed by PCM1, PCM1-N and PCM1-M in PCM1 KO cells. Due to their diffraction-limited size and highly dynamic behavior, Fluorescence Recovery After Photobleaching (FRAP) analysis of PCM1 granules was not feasible. Time-dependent analysis of the internal dynamics of PCM1-N and PCM1-M granules using FRAP revealed that their mobile pools decreased and recovery half-times increased during doxycycline induction. This suggests that the GFP-PCM1-N and GFP-PCM1-M granules became less dynamic over time (Fig. S6A, S6B). Analysis of granule dynamics revealed that GFP-PCM1-N granules demonstrated behaviors such as fusion, splitting, or kiss-and-run, consistent with the heterogeneous biophysical properties of CS granules (Fig. S6C). Notably, the majority of PCM1-N granules exhibited kiss-and-run behavior, where granules touched

but then separated again without altering their shape or fluorescence intensity (Fig. S6C), supporting the predominantly solid-like state of CS granules. Together, these results supports a liquid-to-solid transition during their biogenesis, which has been identified as an assembly mechanism for other membrane-less granules such as RNP granules and pericentrin condensates [49, 52, 53]. Finally, to investigate whether PCM1 granules undergo a similar transition during their biogenesis, we assessed their sensitivity 1,6-HD treatment at 2 h and 16 h after induction. Both granule number and total intensity were more sensitive to 1,6-HD at 2 h compared to 16 h, providing additional evidence that PCM1 granules solidify as they mature (Fig. S6D).

To complement our findings from the *de novo* biogenesis assay with an analysis in a physiological context, we examined the spatiotemporal dynamics of CS disassembly and reassembly during cell division. Specifically, we tracked cell cycle-dependent changes in GFP-PCM1, GFP-PCM1-N and GFP-PCM1-M granule properties using time-lapse imaging (Fig. S7A, S7B). SIR-tubulin was used to label microtubules and centrosomes and to monitor different cell cycle stages (Fig. S3A). A rapid decrease in the total number, volume, and intensity of PCM1 granules upon mitotic entry indicated CS disassembly (Fig.S7A, S7B). As for CS reassembly, a single PCM1 granule formed at the centrosome of each daughter cell around telophase, followed by the formation of PCM1 granules throughout the cytoplasm (Fig. S7A, S7B). The reassembly kinetics upon mitotic exit mirrored those observed in the *de novo* biogenesis assay. Collectively, results from *de novo* and mitotic biogenesis assays show that PCM1 expression initiates *de novo* CS assembly at the centrosome, identifying PCM1 as the nucleating factor and confirming its role as the structural scaffold for CS.

Clients are recruited hierarchically to the PCM1 scaffold

In the multistep pathway for CS assembly, the nucleation of PCM1 would serve as a platform for client recruitment, leading to the assembly of functional CS granules with distinct properties. Alternatively, scaffold and clients may form co-condensates. To distinguish between these scenarios and define the stages of CS assembly, we determined the timing and order of client recruitment following PCM1 scaffold formation. Using the *de novo* biogenesis assay for GFP-PCM1, we fixed cells at various time

points after doxycycline induction, stained the different clients with specific antibodies and determined their colocalization index with PCM1 (Fig. 4A, S8A). For these experiments, we chose nine known CS clients covering a range of CS functions and disease associations: ninein, CEP131, OFD1, CCDC14, KIAA0753, MIB1, CEP290, CEP72 and PIBF1. These clients are involved in processes such as ciliogenesis (CEP72, CEP290), centriole duplication (KIAA0753, CCDC14), and microtubule organization (ninein), and are linked to diseases including microcephaly (PIBF1, ninein), ciliopathy (CEP290, KIAA0753), and oral-facial-digital syndrome (OFD1, KIAA0753) [7, 11, 17, 19, 36, 54-59]. Of note, our analysis was limited by the availability of antibodies that recognize the CS pool of clients.

We measured the Pearson correlation coefficient (PCC) between clients and PCM1 before induction and at 30 min, 2 h, 8 h, and 16 h post-induction. As controls, we used a mix of Alexa 488 and Alexa 568-labeled secondary antibodies, which were used to detect the PCM1 antibody. Their PCC was 0.89, representing the upper limit of our co-localization detection. The lower limit of detection for co-localization was determined by the PCC between non-localizing PCM1 and G3BP1, which was 0.03. For each client, we plotted the mean of their PCC with PCM1 over time (Fig. 4A, 4B). To determine the temporal dynamics of client-PCM1 association, we also quantified the differences in their PCCs across consecutive time points and assigned colocalization strengths to classify clients based on their recruitment times relative to the scaffold (Fig. 4C).

Our analysis revealed that no clients were recruited to the PCM1 scaffold nucleated at the centrosome as early as 10 min, confirming that CS granule formation is initiated solely by PCM1 and does not involve co-condensation with clients (Fig. 4A). By 30 min, several clients including CEP131, CEP290, MIB1, OFD1, and PIBF1 could be detected at the PCM1 granules at or near the centrosome (Fig 4A-C). CEP131 had the highest PCC, identifying it as an early and potentially core client. By 2 h, all clients were detected at the PCM1 granules with varying PCCs (Fig. 4B, 4C). All ten client-PCM1 PCCs increased at both 8 and 16 h, reaching values between 0.3 and 0.6 by 16 h, confirming that CS granules within cells are heterotypic (Fig. 4B, 4C). Over all timepoints, CEP131, MIB1, and PIBF1 had the highest colocalization, CCDC14, OFD1, KIAA0753, and CEP290 showed medium colocalization, and CEP72 and BBS4 showed

the lowest. Importantly, although different clients reached similar PCCs by 16 h or started at similar levels at 30 min, their spatiotemporal recruitment patterns varied significantly (Fig. 4B). This confirms that CS biogenesis involves the hierarchical recruitment of clients following PCM1 scaffold formation.

In addition to PCM1, we fixed and stained cells expressing GFP-PCM1-N and GFP-PCM1-M before and after induction at the same time points. The client recruitment timing and order of the bigger PCM1-N granules largely mirrored those of PCM1 (Fig.S9A-C, S8B). Since PCM1-N formed larger granules, these results strengthen the results obtained from PCM1. One difference we found with PCM1-N was that BBS4, due to its reported interaction with PCM1 through PCM-C, was not recruited to PCM1-N but was to PCM1 (Fig. S9A-C) [33, 60]. Another difference was that PCM1-N granules exhibited stronger client recruitment, with most clients having higher PCCs with PCM1-N compared to PCM1. For example, clients such as ninein, which were not detected in PCM1 granules likely due to their lower abundance, co-localized with PCM1-N granules (Fig. S9A-C).

Strikingly, only one client, CEP290, was recruited to PCM1-M granules even 16 h after dox induction, and it only co-localized with large PCM1-M granules, indicating a low affinity (Fig. S9D). This supports the role of PCM1-M primarily in the self-association of PCM1 and explains why expression of PCM-M did not restore the ciliary defects in PCM1 KO cells (Fig. S4G, S4H)

PCM1 and clients are organized into subdomains within CS granules

Internal organization of other membrane-less organelles such as the core-shell structuring of paraspeckle nuclear bodies or radial-layer architecture pericentriolar material has been proposed as a mechanism for regulating their function via co-regulation of related proteins [61-63]. Given the regulated heterogeneity of CS granule properties, we speculated that CS granules are also spatially organized into subdomains with unique compositions and biophysical properties. To explore this possibility, we examined the ultrastructure of CS granules by mapping the spatial relationships between different PCM1 regions and clients relative to the PCM1 scaffold. Given the sub-diffraction limit diameter of CS granules (~100 nm), we achieved this by

ultrastructure expansion microscopy (U-ExM) and structured illumination microscopy (SIM) followed by 3D quantitative image analysis.

First, we examined the spatial organization of different regions of PCM1 within CS granules (Fig. 5A, 5B). Since PCM1 is a large protein, its different parts may interact with specific regions within CS granules, thereby providing a mechanism for their spatial organization. Similarly, large centrosome proteins like CEP152 and Plp, also rich in coiled-coil domains, were shown to adopt rod-like shapes within pericentriolar material of the centrosome [61, 62]. We investigated the orientation and distribution of PCM1 within CS granules using antibodies to target different regions in various combinations. These regions included the N-terminal 1-254 aa (PCM1-N-Ab), middle region 700-1200 aa (PCM1-M-Ab), and C-terminus 1664-2024 aa (PCM1-C-Ab). We validated the specificity of the antibodies by immunofluorescence and immunoblotting analysis of PCM1 deletion mutants (Fig. S10A-D)

Comparative analysis of fluorescence intensity plots revealed the relative positions of the N and C termini and the M region of PCM1, specifically that they occupy both overlapping and distinct spatial locations within CS granules (Fig. 5A, 5B). They formed irregular, spheroid-like structures. Analysis of their signals across different z-stacks used to generate maximum intensity projections showed the extent of overlap between these signals (Fig. 5B). To determine the spatial organization of scaffold and clients within CS granules, we imaged wild-type RPE1 cells stained with antibodies against PCM1-N and clients (Fig. 5C). We were only able to image two clients, CEP131 and OFD1, for which antibody staining was effective post-U-ExM processing. CEP131 and OFD1 localized to sub-domains distinct from PCM1 (Fig. 5C). CEP131 occupied the core surrounded by the PCM shell, while OFD1 also exhibited some co-localization with the PCM1 shell (Fig. 5C). This analysis confirms that the scaffold and selected clients occupy distinct subdomains.

In addition to endogenous PCM1, we determined the spatial organization of the larger (up to 1 µm in diameter) PCM1-N granules, which facilitate the spatial resolution of CS substructures and increase the detection of low abundance clients by providing more binding sites. The ability of PCM1-N to restore the cilium formation defect in RPE1::PCM1 KO cells demonstrates its functionality and supports its use as a tool for

revealing functionally relevant information about endogenous PCM1 (Fig. S4G, S4H). To this end, we fixed and stained RPE1::PCM1 KO cells inducibly expressing GFP-PCM1-N using antibodies against the nine clients whose timing and sequence of recruitment were studied in the *de novo* biogenesis assay in Fig. 4. Since inducible biogenesis assays revealed an increase in granule size during maturation, we imaged granules of various sizes (0.1 µm to 1 µm) to examine how the spatial distribution of these clients changes during maturation (Fig. S10E).

We observed that GFP-PCM1-N organized into a spheroidal shape, resolvable in granules larger than 0.4 µm (Fig. 5D, S10E, S10F). This is consistent with the spatial organization of PCM1's N terminus within the *in vitro* condensates shown in Fig. 1B. Additionally, while small granules showed spatial differences between PCM1-N and clients within the granules, we could only precisely determine the position of clients relative to the scaffold in granules larger than 0.4 µm (Fig. 5D, S10E) Comparative analysis of intensity profiles of clients relative to PCM1-N revealed that CS clients can be categorized into three groups based on their position within the PCM1-N scaffold: core, patch, and shell. The signals of the core group proteins, including CEP131, KIAA0753 and PIBF1, were surrounded by a continuous shell as stained by GFP-PCM1-N (Fig. 5D, S10E). The shell group, including CEP290 and CEP72, primarily co-localized with GFP-PCM1-N, while Ninein was external to them (Fig. 5D, S10E). Proteins in the patch group, such as CCDC14 and PIBF1, formed small patches distributed within the core and the shell of the PCM1-N scaffold (Fig. 5D, S10E). Finally, proteins including OFD1 and MIB1 were present in both the shell and the core (Fig. 5D, S10E). Collectively, our data reveal a core-shell spatial organization of CS granules, suggesting that the regulation of their internal organization might be a mechanism for compartmentalization and co-regulation of CS functions and associated protein complexes.

CS subdomains and granules have distinct compositions and biophysical properties

The dynamic functions of CS contrast with the predominantly solid state of the PCM1 scaffold. We hypothesize that clients actively involved in CS-mediated functions are

dynamic, whereas those not required for these processes may localize to static substructures. This level of regulation could be achieved through a multiphase organization of CS granules, wherein different subdomains exhibit biophysical properties that vary from liquid to gel to solid states. This heterogeneity is supported by the characterization of PCM1's both liquid and solid-like properties, as shown in Fig. 1A.

We tested the multiphase organization of CS granules using interaction and co-localization experiments. Specifically, we assessed the sensitivity of the CS-client interactions to 1,6-HD. First, we imaged RPE1::PCM1 KO cells expressing PCM1-N granules using SIM to resolve the effects of 1,6-HD on CS architecture (Fig. 5E). The 1,6-HD treatment disrupted the spatial organization of clients and the PCM1-N scaffold, causing the CS to lose their distinct shapes, form smaller spheres, and display significantly altered architecture (Fig. 5E). The sensitivity of clients to 1,6-HD treatment varied, with changes in spatial organization and association with PCM1-N, the most affected being PIBF1, which was lost from PCM1-N granules after treatment (Fig. 5D, 5E). Additionally, co-IP experiments showed that the interactions of CEP131, MIB1 and KIAA0753 with PCM1 were weakened after 1,6-HD treatment, suggesting that their association involved weak hydrophobic interactions characteristic of a liquid-like state (Fig. 6A). However, the interactions of PCM1 with CEP290 was not affected, suggesting its association with a solid-like state. These differences in their biophysical properties may be due to the distinct roles these proteins play in the function and structural integrity of CS, with the former being more dynamic and the latter more stable.

Individual CS granules within the same cell was shown to differ in size and composition, suggesting regulated partitioning of clients among them [13, 36]. To test whether scaffold-client interactions contribute to this regulation, we examined the effect of 1,6-HD on CS compositional heterogeneity in cells. Using PCC analysis, we assessed the extent of colocalization between selected CS clients and PCM1. 1,6-HD treatment significantly decreased the association of all analyzed clients with CS, highlighting their dynamic nature (Fig. 6B,6C). Notably, the reduction in the PCM1 colocalization index ratio varied among clients. Clients such as CEP131, KIAA0753, OFD1 and CCDC14 exhibited 30-55% reduction compared to control, whereas PIBF1, CEP290, and MIB1 showed a 60-80% reduction, and CEP72 and BBS4 had an 80-99%

reduction (Fig. 6B, 6C). This likely reflects the strength of their associations, which might correlate with their dynamicity. Notably, BBS4 and CEP72 are the last two clients to be recruited during CS assembly, highlighting their weaker and more dynamic association (Fig. 4). In contrast to 1,6-HD treatment, RNase treatment did not alter the colocalization index of tested clients with PCM1, except for CEP131, which may rely on RNA for CS localization (Fig.S11A, S11B). These results provide a specificity control for the 1,6-HD experiment and rule out the role of RNA in maintaining CS-client interactions.

Intracellular compositional heterogeneity may allow CS to adapt to different contexts. We propose that CS can remodel in response to various stimuli by releasing or exchanging clients involved in these processes. To test this, we quantified the PCM1 colocalization index for ciliary or basal body proteins in ciliated cells compared to unciliated ones (Fig. 6D, 6E). We selected clients involved in specific stages of primary cilium formation, including positive regulators such as the transition zone component CEP290 and the ciliary axoneme proteins CCDC66, CSPP1, and CEP104, as well as the negative regulator MIB1 [11, 34, 64, 65]. PCCs for CCDC66, CSPP1, CEP104 and CEP290 were reduced in ciliated cells, whereas MIB1 was unaffected (Fig. 6D, 6E). Given the role of the affected proteins in ciliogenesis, this result suggests that rewiring the compositional heterogeneity of CS granules is a mechanism for their dynamic nature and adaptability and for regulating their functions.

Microtubules and CS clients regulate CS assembly and granule properties

To determine the roles of clients and cytoskeleton in CS homeostasis and function, previous studies disrupted or depleted them in cells where CS granules were at steady-state [7, 18, 19]. Therefore, they were limited to uncovering their functions only during maintenance, and for biogenesis. The *de novo* CS biogenesis assay provides a method to spatiotemporally dissect the molecular requirements for CS biogenesis. Specifically, we investigated the roles of clients and microtubules due to their important contributions to CS functions.

To test the role of clients in CS assembly, we chose CEP290 because it is one of the most frequently mutated CS proteins in ciliopathies and was reported to regulate CS

maintenance, suggesting it plays a central role in CS assembly and/or function [55, 57, 66, 67]. To investigate CEP290's role specifically in CS biogenesis, we transfected the RPE1::PCM1 KO cells that inducibly express PCM1 with control or CEP290 siRNAs, which were validated for efficient depletion using immunofluorescence (Fig. S12A). 24 h after transfection, we induced PCM1 expression with doxycycline to trigger CS assembly and fixed the cells at 6, 24 and 48 h post-induction to quantify various CS granule properties (Fig. 7A, 7B). We chose longer induction time points in these assays to differentiate between biogenesis phenotypes that might indicate a defect or just a delay. CEP290-depleted cells formed fewer PCM1 granules and had reduced total granule volume and intensity compared to control cells at all time points (Fig. 7B). The average distance of granules to the centrosome was shorter in CEP290-depleted cells compared to controls, consistent with CEP290's role in inhibiting pericentrosomal clustering of CS (Fig. 7B) [55, 68]. Notably, these differences were less pronounced at 24 h and 48 h, suggesting a delay in CS granule formation that could be due to CEP290 affecting PCM1's phase separation propensity (Fig. 7C). Thus, we tested the effect of CEP290 on the critical concentration threshold for PCM1 by transfecting GFP-PCM1 to control or CEP290-depleted RPE1 cells (Fig. 7C). Supporting our hypothesis, this analysis showed that CEP290 depletion significantly increased PCM1's critical concentration threshold relative to control cells. Taken together, our results identify CEP290 as a factor that promotes CS assembly.

Microtubules might contribute to CS assembly by acting as a scaffold for phase separation or by concentrating PCM1 and clients around centrosomes. To explore this, we performed *de novo* biogenesis assays in RPE1::PCM1 KO cells expressing GFP-PCM1 following microtubule depolymerization by nocodazole treatment for 2 h and 16 h (Fig. 7D, 7E). The average distance of granules from centrosomes was greater in nocodazole-treated cells than in controls at both time points, confirming cytoplasmic redistribution of CS (Fig. 7E). These cells also exhibited fewer PCM1 granules and reduced granule volume and intensity compared to controls, with these defects being less pronounced at 16 h (Fig. 7E). Analysis of steady-state CS properties in nocodazole-treated cells similarly showed a reduction in granule volume, fluorescence

intensity, and number, along with a redistribution of PCM1 granules throughout the cytoplasm. (Fig. S12B).

To complement results from cellular experiments, we examined the impact of taxol-stabilized microtubules on the phase separation behavior of PCM1 *in vitro*. Mixing rhodamine-labeled microtubules with mNG-PCM1 in the BRB80 buffer led to reorganization of microtubules, bringing them closer together and leading to denser networks (Fig. 7F, 7G). We observed larger PCM1 condensates spatially organized into spheroids on microtubules, compared to PCM1-only controls (Fig. 7F, 7G, S12C). We also observed fluorescent puncta containing both PCM1 and tubulin, suggesting co-condensation behavior of these proteins (Fig. 7F, 7G). This confirms tubulin as a PCM1 client, consistent with previous studies that suggest an interaction between PCM1 and free tubulin [69]. Collectively, these results suggest that microtubules regulate CS assembly through their scaffolding and concentration functions. They also further supported the specificity of PCM1 condensates in selectively sequestering CS clients, including tubulin.

Discussion

In this study, we used *in vitro* and cellular assays to determine how functional CS granules with distinct properties form, and elucidate the consequences of their deregulation. Our findings described a hierarchical pathway for the assembly of CS granules. Moreover, we identified mechanisms driving CS assembly and regulation, uncovered sub-compartmentalization of CS granules and revealed direct links between CS homeostasis and function. Finally, our study provides new tools and a conceptual framework for further investigating CS in different contexts.

By combining cellular CS biogenesis assays with a 3D image analysis pipeline, we described the different stages of CS assembly for the first time. Assembly begins with the nucleation of the PCM1 scaffold at the centrosome, followed by stochastic granule formation throughout the cytoplasm and their pericentrosomal clustering. Our data further suggest that nucleation at the centrosome is driven by dynein- and microtubule-dependent transport of PCM1 to the pericentrosomal area, which increases PCM1's concentration above the critical saturation point and promotes granule

formation. Characterization of various PCM1 deletion mutants in these assays revealed multimerization-based phase separation as a mechanism for scaffold assembly, similar to that observed with scaffolding proteins like G3BP1 in stress granules [70-72]. Co-localization of different clients with PCM1 during CS biogenesis revealed varying temporal recruitment kinetics, supporting a model where the PCM1 scaffold serves as a platform for recruiting clients. Finally, biophysical characterization of CS granules suggests liquid-to-solid phase transition during biogenesis. Taken together, these data reveal a hierarchical, multistep assembly pathway for CS granule formation.

Importantly, the hierarchical pathway for CS may explain how granules are organized into subdomains and establish regulated heterogeneity. Variations in the process of recruiting clients, whether individually or collectively, and whether early or late, could diversify and enable CS functions in different contexts. For example, early and late clients likely contribute differently to CS homeostasis. Early clients might possess a high phase-separation propensity that might drive rapid CS core formation. Proteins such as CEP131 and OFD1, which show higher colocalization indices with PCM1, belong to this group. Meanwhile, late proteins may be recruited as discrete modules with dynamic proteins. They might contain functional complexes or co-regulated proteins. An example of this is the BBSome complex, seven-subunit complex that assembles at the CS before its ciliary targeting [73, 74]. Our results identified BBS4, a component of the BBSome, as a late client. Therefore, recruitment of different combinations of the late proteins to CS granules might contribute to CS compositional and functional diversity in different contexts. Future research using time-resolved proteomic profiling of CS during biogenesis is crucial to test these models and systematically profile the recruitment order and properties of clients. A similar approach has successfully identified compositional changes in stress granules during assembly in response to prolonged stress and disassembly [75, 76].

Increasing evidence suggests that the spatial organization of molecules into distinct sub-compartments within membrane-less organelles, such as centrosomes, PML bodies, paraspeckles and stress granules, supports their complex biological functions [63, 77-81]. By high resolution imaging of different clients relative to the scaffold, we discovered that CS granules comprise spatially resolvable substructures with distinct

compositions and biochemical properties. Analysis of different clients involved in various functions revealed a range of localizations, suggesting a core-shell organization along with radial organization for some clients, while others occupied more irregular subdomains. Even PCM1 itself was internally organized within the granules, with its C-terminus facing the cytoplasm externally. This suggests an exciting model where PCM1 might sense cellular signals to regulate CS granule properties. Moreover, we showed that CS granules are multiphase structures where the PCM1 scaffold is solid while clients are dynamically associated with it. Taken together, these CS properties we discovered provide potential mechanisms that enable them to rapidly sequester, modify, or traffic their clients. For example, proteins involved in related pathways or parts of multimeric complexes can be compartmentalized in the same subdomain or partitioned to different subtypes for co-regulation. Moreover, the multiphase organization might enable clients involved in functions elsewhere in the cell to localize to dynamic subdomains to rapidly exchange with other cellular compartments. Future studies, including multiplex imaging of many clients and proteomic profiling of different CS types or subdomains in different contexts, will definitively distinguish among these exciting models.

In addition to cellular assays, we discovered through *in vitro* reconstitution that PCM1 forms granules at physiological protein levels and without crowding agents. Previous *in vitro* studies used high concentrations of smaller PCM1 fragments (326-814 aa, 1072-1337 aa, and 1694-2024 aa fragments at 5-300 μM) and crowding reagents to show that these form liquid-like condensates or undergo gelation [27, 82]. However, these were not physiologically relevant due to the high concentrations used. Our *in vitro* experiments, performed under more physiologically relevant conditions, have several important implications. First, they showed that homotypic interactions of PCM1 alone is sufficient to assemble a scaffold with internal organization, where PCM1-N forms a shell-like structure. Second, *in vitro* PCM1 granules formed co-condensates with MIB1 and tubulin and bound to microtubules. This shows that the granules are functional in compartmentalizing clients and associating with microtubules, which is essential for CS-mediated regulation of protein sequestration and trafficking. These experiments also suggest that clients and microtubules regulate PCM1 granule properties. Finally, *in*

*vitro*reconstitution experiments for CS will be invaluable in future studies that aim to directly test the roles of specific molecules such as kinases, RNA, or cellular extracts in regulating CS assembly and properties.

CS biogenesis assays have allowed us to assess the mechanisms and regulators of CS assembly. First, we determined how different PCM1 regions contribute to scaffold assembly and properties. Our results show PCM1 as a modular protein, with its C-terminal region regulating PCM1-N's ability to drive granule assembly. This regulation may occur through interactions with other proteins, possibly by interacting with PCM1-N and blocking self-association in certain cases or through PTMs such as phosphorylation [38, 83, 84]. Notably, the modular organization of PCM1 may allow it to function as a sensitive switch that initiates granule formation in response to different stimuli such as cell cycle cues. Additionally, cellular reconstitution experiments identified PCM1-M as the critical self-association region for granule assembly. Forced dimerization of PCM1 with FKBP(F36V) led to an increase in size and a decrease in number, resulting in defective Hedgehog pathway activation. This highlights the importance of regulation of PCM1 multimerization in controlling CS granule properties. Taken together, our characterization of the different PCM1 domains for their biophysical properties, and dynamics could provide insights into disease mechanisms, as mutations throughout PCM1 have been implicated in schizophrenia, and fusions of its C-terminal truncations with kinases have been identified in leukemia [23, 85-90].

We also investigated how the cytoskeleton and clients regulate CS properties. Previously, clients had only been studied as proteins regulated by CS, and microtubules were examined for their role in CS transport [7, 9, 11, 24, 37, 55]. We investigated how disrupting microtubules or depleting a specific client, CEP290, affects CS properties during biogenesis. Our results showed that both treatments led to a decrease in CS granule size and number, identifying them as regulators that promote CS assembly. Microtubules may promote CS assembly by concentrating PCM1 molecules, either by acting as a scaffold or by facilitating their pericentrosomal concentration, thus lowering Csat and promoting the fusion of granules. The increase in PCM1 granule size observed with microtubules in *in vitro* experiments further supports this model. Given the emerging data on the role of phase separation in regulating microtubule-based

processes, future studies exploring how PCM1 might influence microtubules would be of great interest [91, 92]. Regarding clients, they may interact with PCM1 and other clients, contributing to the collective interactions that drive CS granule formation by lowering the Csat of PCM1. Additionally, our systematic analysis of proteins expressed similarly to PCM1 during *de novo* CS assembly suggest potential new co-regulatory modules and functional complexes, such as those associated with actin, involved in CS assembly. The identification of clients and the cytoskeleton as active regulators of CS homeostasis is crucial, as it positions CS as a cellular compartment that could be disrupted in diseases associated with cytoskeletal and client abnormalities, such as ciliopathies and cancer. Future studies with disease mutants of PCM1 or clients using the *in vitro* and cellular assays we developed will provide insight into these questions.

Materials and Methods

Plasmids

Full-length cDNAs of *Homo sapiens* PCM1 (GenBank accession no: NP_006188.4) and *Homo sapiens* MIB1 (GenBank accession no: NM_020774.4) were used. Primers used for cloning are included in Table S2. Full-length cDNAs for human PCM1 and its deletion mutants (nucleotides GFP-PCM1: 1-6072 bp, GFP-PCM1-N: 1:3600 bp and GFP-PCM1-M: 2100-3600 bp, GFP-PCM1-NS: 1:2100 bp and GFP-PCM1-C: 3600-6072 bp) were amplified by PCR and cloned into pDONR221 plasmid using Gateway technology (Thermo Fisher Scientific). The ORF of GFP-PCM1, GFP-PCM1-N and GFP-PCM1-M was amplified by PCR and cloned into pDONR221. Subsequent Gateway recombination reactions using pInducer20 and pEF-FRT-LapC DEST (provided by Max Nachury, UCSF) were performed. To generate FLAG expression vector, was cloned into the pCDNA5.1-FRT/TO-Flag-miniTurboID vector (a gift from the Bettencourt-Dias laboratory at IGC Gulbenkian) using AscI and NotI restriction sites in the forward and reverse primers, respectively.

For protein purification, cDNAs encoding GFP, mNeonGreen, PCM1-M (2100-3600 bp), and PCM1-C (4993-6073 bp) were amplified by PCR and initially cloned into the pDONR221 vector. Subsequent cloning was performed into pDEST-His-MBP and pDEST-GST vectors using Gateway technology. Full-length cDNA for human PCM1

was cloned into pCDH-EF1-mNeonGreen-T2A-Puro lentiviral expression plasmid using BamHI and NotI restriction sites in forward and reverse primers, respectively. Full length MIB1 was cloned to pCDH-EF1-mScarlet-T2A-Puro lentiviral expression plasmid using BamHI and NotI restriction sites in forward and reverse primers, respectively. The mScarlet-MIB1 was amplified from the pCDH-mScarlet-MIB1 plasmid and cloned into the pDEST-His-MBP vector via Gateway cloning. mNeonGreen-tagged PCM1 was amplified from the pCDH-mNeonGreen-PCM1 plasmid and subsequently cloned into the pFastBac-His-MBP vector using Gateway cloning.

For inducible dimerization system, FKBP(F36V) was amplified from the pCDNA3.1(+)-miniTurboID-6xGGSGlinker-FKBPF36V-2xHA plasmid (Addgene plasmid #200641) and subsequently cloned into the pCDH-EF1-mNeonGreen-PCM1-T2A-Puro lentiviral expression plasmid using the NotI enzyme in forward and reverse primers.

Cell culture and transfections

Human telomerase-immortalized retinal pigment epithelium cells (hTERT-RPE1, ATCC) were cultured in Dulbecco's Modified Eagle's Medium/F12 50/50 medium (Pan Biotech) supplemented with 10% fetal bovine serum. Human embryonic kidney (HEK293T, ATCC) and human cervical carcinoma cells (HeLa, ATCC) were cultured in DMEM medium supplemented with 10% FBS. All cell lines were maintained in a humidified incubator at 37°C with 5% CO2 and confirmed negative for mycoplasma using a PCR-based test. RPE1::PCM1 KO cell lines were previously described and validated [10]. To generate Hela::PCM1 KO cells, we used the gRNA plasmids and followed the protocol previously described[10].

HEK293T and HeLa cells were transfected with plasmids using 1 µg/µL polyethylenimine. For siRNA transfections, cells were seeded onto coverslips at 70% confluency and transfected with 50 nM siRNAs in two sequential transfections using Lipofectamine RNAiMAX in OPTIMEM according to the manufacturer's instructions. CEP290 depletion was achieved using a previously validated siRNA sequence (5'-GAUACUCGGUUUUUACGUAUUUU-3') [37]. Control siRNA (Ambion, Cat. #4390847) was used as a control. 48 h post-transfection, cells were induced with 1 µM doxycycline and fixed at the specified times.

High Five (Hi-5) insect cells were cultured in serum-free Insect-XPRESS medium, while Spodoptera frugiperda (Sf9) insect cells were grown in Spodopan supplemented with 10% fetal bovine serum for growth conditions. For transfections and virus/protein production, Sf9 cells were cultured in serum-free medium. All insect cell lines were maintained at 27°C with 5% CO2 in a humidified incubator, either as adherent or suspension cultures equipped with a rotator shelf. Sf9 cells were transfected with plasmids using FuGENE HD for baculovirus production.

Lentivirus production and cell transduction

Lentivirus was generated as previously described, using pInducer20-GFP-PCM1, pInducer20-GFP-PCM1-N, pInducer20-GFP-PCM1-M and pCDH-mNG-PCM1 FL-FKBP(F36V) plasmids as transfer vectors [93]. For infection, 1×10^5 RPE1::PCM1 KO cells were seeded in 6-well tissue culture plates the day before the infection. These cells were infected with 1 ml of viral supernatant the following day. 24 h post-infection, the medium was replaced with complete medium. 48 h post-infection, the cells were split and subjected to selection. Cells infected with pInducer20-carrying lentivirus were selected in the presence of 1 mg/ml neomycin (G-418), and those infected with pCDH-mNG-carrying lentivirus were selected with 2 µg/ml puromycin. Both selections were carried out for 5–7 days until all control cells died. After determining the infection efficiency in the heterogeneous pool using immunofluorescence experiments, the cells were trypsinized and serial dilutions were performed in normal growth medium. Colonies that formed within 10–14 days were then trypsinized and expanded for screening for colonies expressing the fusion proteins at low levels using immunofluorescence and Western blotting.

Drug treatments

All chemicals used in this manuscript are listed in Table S2.For the 1,6-Hexanediol treatment, cells were incubated in complete media containing 5% 1,6-Hexanediol for 5 min. Following incubation, cells were washed twice with PBS and then fixed. To induce stress granules, cells were treated with 50 mM NaAsO2 for 1 h. The

sensitivity of these cells to 1,6-Hexanediol was subsequently assessed by treating them with 5% 1,6-Hexanediol for 5 min.

For the nocodazole treatment, inducible RPE1::PCM1 KO cells expressing GFP-PCM1 were subjected to two different treatment protocols. For the 2-h assay, cells were simultaneously treated with 5 µg/ml nocodazole for 1 h and induced with 1 µM doxycycline for 2 h. For the 16-h assay, cells were simultaneously induced with 1 µM doxycycline and 5 ng/ml nocodazole for 16 h. After treatments, the cells were washed with PBS and fixed.

RNase treatment was performed by incubating cells in complete media mixed with 100 µg/ml RNase I and RNase A. Cells were incubated in RNase mixture for 1 h, followed by washing with PBS and fixation.

For mitotic synchronization, cells were treated with 400 µM mimosine for 24 h to synchronize them to the G1 phase, followed by 100 µM STLC for 16 h to synchronize them to mitosis. Cells were harvested and analyzed via Western blotting for PCM1 and Vinculin.

For ciliation experiments, cells were incubated in low-serum medium (0.5% serum) 24 or 48 h after reaching 100% confluency. For Hedgehog pathway activation experiments, cells were treated with 50 nM SAG for 24 h to activate the Hedgehog signaling pathway following serum starvation.

To induce dimerization of PCM1, RPE1::PCM1 KO cells stably expressing mNG-PCM1-FKBP(F36V) were treated with 250 nM B/B Homodimerizer (AP20187) for a minimum of 4 h. For dissociation of the dimerized granules, cells were washed twice with PBS post-treatment and subsequently treated with 1 µM wash-out ligand for at least 1 h. The duration of treatment varied based on the experiment. For cilium assembly, the treatment lasted 24 h; for Sonic hedgehog stimulation, 48 h; and for live imaging of mitosis, 18 h.

Immunofluorescence, antibodies and microscopy

Cells were grown on coverslips, washed twice with PBS and fixed with ice-cold methanol at −20°C for 3 min or 10 min. After washing twice with PBS, cells were blocked with 3% BSA in PBS plus 0.1% Triton X-100 and incubated with primary

antibodies in blocking solution for 1 h at room temperature. Cells were washed three times with PBS and incubated with secondary antibodies and DAPI at 1:2000 for 45 min at room temperature. Following three washes with PBS, cells were mounted using Mowiol mounting medium containing N-propyl gallate. Full list of primary and secondary antibodies used for immunofluorescence experiments in this study are listed Table S2.

Confocal microscopy was performed with a Leica TCS SP8 or Stellaris 8 laser-scanning inverted confocal microscope system equipped for four-color imaging with 405, 488, 561, and 633 nm laser lines, four detection channels (1 photomultiplier tube and 3 Hybrid Detectors), HC PL APO CS2 63 × 1.4 NA and HC PL APO CS2 40 × 1.3 NA oil objectives and an incubation chamber. Pinhole diameter was set to 1 µm. Images were acquired at 20–50 focal planes with 0.2–0.5 µm z-spacing, line averaging set to 2–3 and 400 Hz unidirectional xyz scan mode. An image format of 1,024 × 1,024 pixels and an additional 2–4× optical zoom was used for sample acquisition. The system was controlled with the Leica Application Suite X Software (Leica). Post-processing was performed using the Huygens Professional (Scientific Volume Imaging) or LAS X Lightning.

3D-SIM imaging was performed using Elyra 7 with Lattice SIM^2 (Carl Zeiss Microscopy) with a Plan-Apochromat 63×/1.4 Oil DIC M27 objective, 405/488/561/633 nm laser illumination, and standard excitation and emission filter sets. A sCMOS (version 4.2 CL HS) camera was used to acquire images with 110 nm z-spacing over 5–10-µm thickness. Laser powers at the objective focal plane were in the 2–12% range, exposure time was between 50 and 250 ms, and camera gain values were between 5 and 50 during image acquisition. The raw data were reconstructed using the SIM module of ZEN Black Software. Channel alignment was conducted using a calibrated file generated from super-resolution Tetraspec beads (Carl Zeiss Microscopy).

For time lapse imaging, doxycycline-inducible RPE1-PCM1 KO cell lines expressing GFP-PCM1, GFP-PCM1-N, and GFP-PCM1-M were seeded onto 35-mm glass-bottom dishes. After the addition of 1 µg/ml Doxycycline, imaging was performed using a Stellaris 8 confocal microscope equipped with an HC PL APO CS2 63x 1.4 NA oil objective, maintaining a 5% CO2 atmosphere at 37°C. Imaging was performed with the same acquisition setting and conditions for replicates. For time-lapse imaging of CS

dimerization and reversing dimerization, cells were cultured in Ibidi µ-Slide 8-well dishes and imaged at 37°C and 5% CO2. Initially, images were captured every 2 min for one hour, then every 20 min up to 4 h, using a 0.5 µm step size in a 512 x 512 pixel format. Cells received treatments with dimerizer and washout ligands between the first two frames.

Ultrastructural Expansion Microscopy

Ultrastructure Expansion Microscopy (U-ExM) was performed as previously described [94]. RPE1 cells were cultured on 12 mm coverslips in a 24-well plate. Coverslips were incubated in a 1.4% formaldehyde / 2% acrylamide (2X FA/AA) solution in 1X PBS for 5 h at 37°C. The cells were then embedded in a gel prepared using Monomer Solution (sodium acrylamide 38% (w/w), 12.5 µl acrylamide, 2.5 µl BIS, and 5 µl 10X PBS), supplemented with TEMED and 0.5% APS and polymerized for 1 h at 37°C. Denaturation was carried out at 95°C for 90 min, followed by staining with primary antibodies for 3 h at 37°C. The gels were then washed three times for 10 min at RT with PBS-T. Secondary antibody incubation was performed for 2.5 h at 37°C, followed by three additional 10-minute washes with PBS-T at RT. Before imaging, gels were expanded in 100 ml dH_2O three times. The expansion factor was determined by measuring the gel diameter with a ruler and dividing it by the original 12 mm diameter. Gels were cut into smaller pieces and mounted onto 24 mm coverslips coated with Poly-D-lysine. Imaging was performed using a Leica Stellaris confocal microscope with 0.30 µm z-intervals, and images were deconvolved using Lightening mode.

Image Analysis

1- Quantification of granule properties and critical saturation concentrations

Granule properties, including number, size, and intensity, were quantified using GFP-PCM1 or endogenous PCM1 signals with the surface creation function in Imaris software (Bitplane, Oxford Instruments) provided by Emory University's Integrated Cellular Imaging Core. Surfaces were detected based on intensity thresholding, and diameters were estimated using the software's built-in algorithm. Manual corrections were made as necessary to ensure accurate segmentation. Centrosomes were

detected and analyzed using the Spot Detection module in Imaris, based on gamma-tubulin or centrin 2 signals. Spot sizes were set based on the approximate diameter of centrosomes (~1 µm), and an intensity threshold was applied for automatic detection. Manual curation was employed to remove false positives. For each cell, data related to volume (µm^3), average volume (µm^3), intensity sum, average intensity, distance to spots, sphericity, and surface count were directly exported as Excel files from the software. Data from these files were compiled and analyzed using GraphPad.

Critical saturation concentration values were determined based on relative protein concentrations calculated from total fluorescent intensities and volumes. Initially, individual PCM1 granules were rendered for each cell using the surface creation tool from the GFP signal, with segmentation performed without selecting the smoothing option. The 'Split Touching Objects' function (morphological split) was used to separate individual granules in contact with each other. Different threshold values differentiated granular from cytoplasmic PCM1. Both were rendered in 3D, and their total intensity and volume values were exported. Intensity values were normalized to the maximum fluorescent intensity for each biological replicate. The concentration of granules was calculated by dividing their total intensity by their total volume (µm^3) for each cell. To calculate the concentration of cytoplasmic PCM1, the intensity and volume of granules within the surface were subtracted from the total intensity and volume of the whole cytoplasm, and the resulting ratio was calculated. The critical saturation concentration of PCM1 granules was determined as the average concentration value across granules for each cell line.

Pearson’s coefficient for the colocalized volume in each cell was calculated using the 'Coloc' module of Imaris. The first channel was assigned to endogenous PCM1 or GFP-PCM1, and the second channel was assigned to client proteins. Thresholding parameters were manually chosen to specifically select PCM1 granules. A new channel was created using the 'Build Coloc Channel' function. The results were directly exported from Imaris via the Image Properties tab as Excel files, and the data were analyzed using GraphPad.

Quantification of granule properties in in-vitro experiments was conducted using Aivia software (Leica Microsystems). Prior to analysis, 3D raw image stacks underwent

background subtraction to enhance granule segmentation by the machine learning tool. Granule detection was performed using the Object Detection module in Aivia, with intensity thresholding and size filtering optimized to exclude non-specific signals and background noise. The segmentation parameters were fine-tuned to accurately eliminate individual granules based on their fluorescence intensity and size. The volume value for each granule was exported and analyzed in GraphPad Prism. The conversion of condensate volume to radius was performed assuming a perfect spherical shape.

2- Line profile calculations

3D images were opened in ImageJ in their native format. The entire z-stack was projected using the '3D Project' function (Image > Stacks > 3D Project). A line of varying lengths was drawn to correspond to the granule sizes. The intensity across the line was calculated using the Analyze > Plot Profile command. The exported intensity values were used to create graphs in GraphPad.

3- Analysis of centrosomal and ciliary levels of proteins

All centrosomal and ciliary level quantifications were performed in ImageJ. Regions of interest (ROIs) around the centrosome or the primary cilium were determined using markers for the centrosome (gamma-tubulin or centrin 2) or the primary cilium (Arl13b, acetylated tubulin, or glutamylated tubulin), and the corresponding signals were quantified. The cytoplasmic signal was subtracted from this value for each individual cell. Statistical analysis was conducted by normalizing these values to the mean for each biological replicate.

Fluorescence recovery after photobleaching analysis

For stable lines, RPE1::PCM1 KO cells expressing GFP-PCM1-N or GFP-PCM1-M were cultured in coverglass-bottom dishes (Laboratory-Tek II Chamber) and induced with 1 µm doxycycline for 20 min, 1 h, and 16 h. Photobleaching experiments were performed using Leica SP8 confocal laser scanner (Leica SP8) a Plan Apofluar 63 × 1.4 NA objective and a scan zoom of 2.5. Cells were kept at 37°C with 5% CO_2 during the imaging. A z-stack of 2.7 µm with 0.3 µm step size was taken during pre- and post-bleaching cilium FRAP experiments. One stack of images was captured before photobleaching, followed by photobleaching done in ten iterations with 488-nm Argon

laser with 100% power in the defined ROIs. Post-bleaching stacks were captured every 8 seconds for 5 min for RPE1 cells. The relative fluorescence intensities were calculated from the maximum projection files using Fiji and plotted against time. Recovery graph quantifications, t-half, and mobile pool quantifications were done using the equations as previously described [95].

Cell lysis and immunoblotting

Cells were lysed in RIPA buffer containing 50 mM Tris-HCl, 150 mM NaCl, 1.0% (v/v) Triton X-100, 0.5% (w/v) sodium deoxycholate, 1.0 mM EDTA, 0.1% (w/v) SDS, and protease inhibitors. Lysis was carried out for 30 min at 4°C, followed by centrifugation at 13,000 g for 15 min. Protein concentration in the supernatant was measured using the Bradford assay (Bio-Rad Laboratories). For immunoblotting, equal amounts of proteins were loaded and separated by SDS-PAGE, transferred onto nitrocellulose membranes, and blocked with 5% milk in TBS-T for 1 h at room temperature. Membranes were incubated overnight at 4°C with primary antibodies diluted in 5% BSA in TBS-T, followed by three 5-minute washes in TBS-T. They were then incubated with secondary antibodies for 1 h at room temperature, washed again, and visualized using the LI-COR Odyssey Infrared Imaging System at 680 and 800 nm (LI-COR Biosciences). Full list of primary antibodies used for western blot experiments in this study are listed Table S2. Secondary antibodies used for Western blotting experiments were IRDye 680- and IRDye 800-coupled and were used at 1:15,000 (LI-COR Biosciences).

Solubility assay

HEK293T::PCM1 KO cells were co-transfected with GFP-FL, GFP-PCM1-N, GFP-PCM1-C, GFP-PCM1-M, or GFP-PCM1-NS. 48 h post-transfection, cells were lysed using a buffer composed of 50 mM HEPES (pH 8), 100 mM KCl, 2 mM EDTA, 10% glycerol, 0.1% Nonidet™ P40, and a protease inhibitor cocktail. After lysis for 30 min at 4°C, lysate was centrifuged at 14,000 rpm for 15 min. The protein concentration

of the resultant supernatants was measured using Bradford solution (Bio-Rad Laboratories). Both the supernatant fraction and the insoluble pellet fraction were resuspended in SDS-containing sample buffer and analyzed by immunoblotting.

Pulldown experiments

For FLAG pulldown experiments, HEK293T-PCM1 KO cells were co-transfected with Flag-PCM1 along with GFP, GFP-PCM1-N, GFP-PCM1-C, GFP-PCM1-M or GFP-PCM1-NS. After 48 h, the cells were washed and lysed using Flag pulldown buffer (50 mM HEPES, pH 8, 100 mM KCl, 2 mM EDTA, 10% glycerol, 0.1% NP-40, freshly supplemented with 1 mM DTT and protease inhibitors: 10 µg/ml Leupeptin, Pepstatin, and Chymostatin, and 1 mM PMSF) for 30 min. Lysates were centrifuged at 13,000 rpm for 10 min at 4°C, and the supernatants were collected. 100 µl aliquot from each sample was saved as input, while the remaining supernatant was immunoprecipitated overnight at 4°C using Anti-FLAG M2 agarose beads (Sigma Aldrich).

Protein expression and purification

For the expression of His-MBP-mNG-PCM1, 500 ml of Hi5 cells at a density of 1 × 10^6 cells/ml were infected with P1/P2 baculovirus produced in Sf9 cells at an MOI of 1. The cells were harvested 48 h post-infection. For the expression of His-MBP-mScarlet-MIB1, BL21 Rosetta cells were induced with 0.5 mM IPTG at an OD600 of 0.5, incubated at 18 °C for 18 h and harvested.

For protein purification, cells were lysed using ice-cold lysis buffer (50 mM NaH2PO4, 500 mM NaCl, 20 mM imidazole, 0.5% Triton, 10% glycerol, 0.5 mM arginine, pH 7.0) supplemented with 1 mM PMSF, 5 mM beta-mercaptoethanol, and a protease inhibitor cocktail. The lysate was sonicated, then clarified by centrifugation at 14,000 rpm for 45 min at 4°C. Proteins were bound to Ni-NTA beads (Thermo Scientific), eluted with 300 mM imidazole following the manufacturer's instructions (Qiagen), and dialyzed overnight at 4°C into storage buffer. MIB1 was dialyzed into buffer containing 20 mM HEPES (pH 7.0), 500 mM NaCl, and 1 mM DTT. PCM1 was dialyzed into a buffer with 20 mM HEPES (pH 7.0), 150 mM NaCl, and 1 mM DTT using a PD-10 desalting column. The proteins were further concentrated using Amicon Ultra

30K centrifugal filter devices (Millipore). Finally, 10 µl aliquots of the protein were snap-frozen in liquid nitrogen and stored at −80 °C.

In vitro phase separation assay

To assay phase separation behavior, purified His-MBP-PCM1 was diluted to varying concentrations (0.5 µM, 1 µM, 2 µM) in assay buffer. This buffer consisted of 10 mM HEPES, 0.1 mM EDTA, 2 mM DTT, and varying concentrations of NaCl (150 mM, 500 mM). The samples were also prepared in the presence of DMSO or 5% 1,6-hexanediol (ChemCruz, sc-237791). After a 5 min incubation, 25 µL of each mixture was loaded into an imaging chamber. This chamber was constructed by mounting HCl-treated glass coverslips on cover slides with strips of double-sided tape, as previously described (Alberti et al, 2018). Imaging was performed using a Leica SP8 confocal microscope with an HC PL APO CS2 63× 1.4 NA oil objective. Additionally, conditions including 0.15 mM His-MBP-mScarlet-MIB1 were examined using the same buffer and experimental setup. For microtubule experiments, 1 mM Taxol-stabilized microtubules were analyzed in BRB80 buffer (80 mM PIPES pH 6.8, 1 mM EGTA, 1 mM MgCl2) using the same setup. To generate Taxol-stabilized microtubules, purified bovine tubulin was first precleared at 90,000 rpm for 5 min at 4°C using a Beckman Coulter Optima MAX-XP Benchtop Ultracentrifuge with TLA110 Rotor. The cleared tubulin was then diluted to a concentration of 2 mg/mL and polymerized by incubating with 20 µM Taxol in stepwise increments of 0.02 µM, 0.2 µM, and 2 µM at 37°C for 30 min.

For TIRF analysis, microscopy slides were prepared by mounting HCl-treated glass coverslips onto the cover slide using strips of double-sided tape. Bovine brain tubulin, both non-labeled and labeled with Alexa Fluor™ 568 NHS Succinimidyl Ester (Thermo, 20003), was used to reconstitute a 1 µM Rhodamine Microtubule mixture, comprising 10% labeled tubulin mixed with non-labeled tubulin. Anti-β-tubulin antibody was applied to the salinized cover slide surface, which had been prepared using trichloroethylene and dichloromethylsilane. Excess antibody was removed by washing with 0.2 mg/mL κ-casein and Pluronic-127. The Rhodamine microtubules were then attached to the antibody-coated, salinized cover slide surface and subsequently washed first with 2 mg/mL κ-casein, followed by 0.05 mg/mL κ-casein. A solution of 140 nm His-

MBP mNG-PCM1 supplemented with a GOC scavenger mix (glucose oxidase, catalase, BME, glucose in BRB80) and κ-casein was flowed in and incubated for 3 min to allow binding of His-MBP-mNG-PCM1 to the microtubules. The edges of the cover slide were sealed with nail polish and the samples were imaged at 30°C using a Zeiss ELYRA 7 microscope with a 100X TIRF objective.

Mass spectrometry

For the quantitative comparison of WT and knockout cells, snap-frozen cell pellets of 1×10^6 cells were resuspended in 50 µl PBS followed by the addition of 50 µl of 1% SDS in 100 mM HEPES, pH 8.4 and protease inhibitor cocktail (Roche, #11873580001). Samples were heated to 95°C for 5 min and then transferred on ice. Samples were treated with benzonase at 37°C for 1 h to degrade DNA. Protein concentrations were determined and adjusted to 1 µg/µl.

For the mass spectrometric analysis, 10 µg of lysate were subjected to an in-solution tryptic digest, following a modified version of the Single-Pot Solid-Phase-enhanced Sample Preparation (SP3) technology [96, 97]. 20 µl of a slurry of hydrophilic and hydrophobic Sera-Mag Beads (Thermo Scientific, #4515-2105-050250, 6515-2105-050250) were mixed, washed with water and were then reconstituted in 100 µl water. 5 µl of the prepared bead slurry were added to 50 µl of the eluate following the addition of 55 µl of acetonitrile. All further steps were prepared using the KingFisherApex System (Thermo Scientific). After binding to beads, beads were washed three times with 100 µl of 80% ethanol before they were transferred to 100 µl of digestion buffer (50 mM Hepes/NaOH pH 8.4 supplemented with 5 mM TCEP, 20 mM chloroacetamide (Sigma-Aldrich, #C0267), and 0.25 µg trypsin (Promega, #V5111)). Samples were digested overnight at 37°C, beads were removed, and the remaining peptides were dried down and subsequently reconstituted in 10 µl of water.

50 µg of TMTpro (Thermo Scientific, #A44522, #AA52048) label reagent was dissolved in 4 µl of acetonitrile [98]. TMT labelling reagent was added to tryptic peptides following incubation for 1 h at room temperature. Excess TMT reagent was quenched by the addition of 4 µl of an aqueous solution of 5% hydroxylamine (Sigma, 438227). Mixed peptides were subjected to a reverse phase clean-up step (OASIS HLB 96-well

µElution Plate, Waters #186001828BA). Peptides were subjected to an offline fractionation under high pH conditions [96]. The resulting 12 fractions were analyzed by LC-MS/MS on a Lumos system (Thermo Scientific).

Peptides were separated using an Ultimate 3000 nano RSLC system (Dionex) equipped with a trapping cartridge (Precolumn C18 PepMap100, 5 mm, 300 µm i.d., 5 µm, 100 Å) and an analytical column (Acclaim PepMap 100. 75 × 50 cm C18, 3 mm, 100 Å) connected to a nanospray-Flex ion source. The peptides were loaded onto the trap column at 30 µl per min using solvent A (0.1% formic acid) and eluted using a gradient from 2 to 80% Solvent B (0.1% formic acid in acetonitrile) over 2 h at 0.3 µl per min (all solvents were of LC-MS grade). The Orbitrap Fusion Lumos was operated in positive ion mode with a spray voltage of 2.2 kV and capillary temperature of 275 °C. Full scan MS spectra with a mass range of 375–1500 m/z were acquired in profile mode using a resolution of 120,000 with a maximum injection time of 50 ms, AGC operated in standard mode and a RF lens setting of 30%.

Fragmentation was triggered for 3 s cycle time for peptide like features with charge states of 2–7 on the MS scan (data-dependent acquisition). Precursors were isolated using the quadrupole with a window of 0.7 m/z and fragmented with a normalized collision energy of 34%. Fragment mass spectra were acquired in profile mode and a resolution of 30,000. Maximum injection time was set to 94 ms and AGC target to custom. The dynamic exclusion was set to 60 s.

Mass spectrometry data analysis

For the global proteomics data analysis, the raw output files of FragPipe (protein.tsv files) were processed using the R programming environment (ISBN 3-900051-07-0). Initial data processing included filtering out contaminants and reverse proteins. Only proteins quantified with at least 2 razor peptides (with Razor.Peptides >= 2) were considered for further analysis. 6605 proteins passed the quality control filters. In order to correct for technical variability, batch effects were removed using the 'removeBatchEffect' function of the limma package on the log2 transformed raw TMT reporter ion intensities ('channel' columns) [99]. Subsequently, normalization was performed using the 'normalizeVSN' function of the limma package (VSN - variance

stabilization normalization - PMID: 12169536). Differential expression analysis was performed using the moderated t-test provided by the limma package [99]. The model accounted for replicate information by including it as a factor in the design matrix passed to the 'lmFit' function. Proteins were annotated as hits if they had a false discovery rate (FDR) below 0.05 and an absolute fold change greater than 1.5. Proteins were considered candidates if they had an FDR below 0.2 and an absolute fold change greater than 1.5. Clustering with all hit proteins based on the median protein abundances normalized by median of control condition was conducted to identify groups of proteins with similar patterns across conditions. The 'k means' method was employed, using Euclidean distance as the distance metric and 'ward.D2' linkage for hierarchical clustering. The optimal number of clusters (10) was determined using the Elbow method, which identifies the point where the within-group sum of squares stabilizes. Gene ontology (GO) enrichment analysis was performed using the 'compareCluster' function of the 'clusterProfiler' package (PMID: 22455463), which assesses over-representation of GO terms in the dataset relative to the background gene set. Enrichment was conducted for the following GO categories: Cellular Component (CC), Molecular Function (MF), and Biological Process (BP). The analysis was performed using 'org.Hs.eg.db' as the reference database. The odds ratio ('odds_ratio') for each GO term was calculated by comparing the proportion of genes associated with that term in the dataset ('GeneRatio') to the proportion in the background set ('BgRatio'). An odds ratio greater than 1 indicates that the GO term is enriched in the dataset compared to the expected background.

For the mass spectrometry analysis of purified proteins, two biological replicates of His-MBP-mNG-PCM1 were each run as two technical replicates, yielding a total of four runs. The peptide spectrum match (PSM) values for each identified protein were normalized by dividing them by the total sum of PSM values for their respective technical replicate. The normalized PSM values were then divided by the amino acid length of each protein to account for protein size. Proteins identified in only one technical replicate out of the two biological replicates across the four runs were eliminated as nonspecific reads. The percentage of His-MBP-mNG-PCM1 in the purified protein sample was calculated from the final normalized PSM values.

Statistical analysis

Statistical significance and p-values were assessed using Prism 7 software (GraphPad Software, La Jolla, CA). For comparisons between two groups with a normal distribution, a two-tailed Student's t-test was used, while one-way analysis of variance (ANOVA) was applied for comparisons involving more than two groups. The sample size (n) represents the number of experimental replicates for each sample and condition. Error bars in the graphs indicate the standard deviation (SD), and statistical significance levels were denoted as follows: ns: $P>0.05$, *:$P<0.05$, **:$P<0.01$, ***:$P<0.001$ and ****:$P<0.0001$.

Acknowledgements

We acknowledge the CytoLab members for their insightful feedback on this work. We thank Dila Gulensoy for cloning plasmids for expressing GFP-fusions of PCM1-NS, PCM1-N and PCM1-C. We also acknowledge use of the services and facilities of the EMBL Proteomics Facility, Koc University Proteomics Facility, Koc University Animal Facility and Istanbul University Animal Facility. This work was supported by the Emory University Emory Integrated Cellular Imaging Core Facility (RRID:SCR_023534) for the usage of Imaris Software. This project has received funding from European Union's Horizon Europe research and innovation program under the European Research Council Starting grant agreement "SatelliteHomeostasis" to ENF. This work was also supported by EMBO Installation Grant 3622 and Young Investigator Award and Istanbul Development Agency Grant to ENF. During the preparation of this work the authors used ChatGPT in order to improve language and punctuation, with caution and selectivity. After using this tool, the authors thoroughly reviewed and edited the content as needed and take full responsibility for the content of the publication.

Competing interest

The authors declare no competing interests.

References

1. Banani, S.F., Lee, H.O., Hyman, A.A. & Rosen, M.K. Biomolecular condensates: organizers of cellular biochemistry. *Nat Rev Mol Cell Biol* **18**, 285-298 (2017).
2. Hyman, A.A., Weber, C.A. & Julicher, F. Liquid-liquid phase separation in biology. *Annu Rev Cell Dev Biol* **30**, 39-58 (2014).
3. Li, Y. *et al.* Membraneless organelles in health and disease: exploring the molecular basis, physiological roles and pathological implications. *Signal Transduct Target Ther* **9**, 305 (2024).
4. Woodruff, J.B., Hyman, A.A. & Boke, E. Organization and Function of Non-dynamic Biomolecular Condensates. *Trends Biochem Sci* **43**, 81-94 (2018).
5. Gomes, E. & Shorter, J. The molecular language of membraneless organelles. *J Biol Chem* **294**, 7115-7127 (2019).
6. Li, P. *et al.* Phase transitions in the assembly of multivalent signalling proteins. *Nature* **483**, 336-340 (2012).
7. Begar, E., Seyrek, E. & Firat-Karalar, E.N. Navigating centriolar satellites: the role of PCM1 in cellular and organismal processes. *FEBS J* 292(4), 688–708 (2024) (2024).
8. Hall, E.A. *et al.* Centriolar satellites expedite mother centriole remodeling to promote ciliogenesis. *Elife* **12, e79299** (2023).
9. Kubo, A., Sasaki, H., Yuba-Kubo, A., Tsukita, S. & Shiina, N. Centriolar satellites: molecular characterization, ATP-dependent movement toward centrioles and possible involvement in ciliogenesis. *J Cell Biol* **147**, 969-980 (1999).
10. Odabasi, E., Gul, S., Kavakli, I.H. & Firat-Karalar, E.N. Centriolar satellites are required for efficient ciliogenesis and ciliary content regulation. *EMBO Rep* 20, e47723 (2019).
11. Wang, L., Lee, K., Malonis, R., Sanchez, I. & Dynlacht, B.D. Tethering of an E3 ligase by PCM1 regulates the abundance of centrosomal KIAA0586/Talpid3 and promotes ciliogenesis. *Elife* **5** (2016).
12. Aydin, O.Z., Taflan, S.O., Gurkaslar, C. & Firat-Karalar, E.N. Acute inhibition of centriolar satellite function and positioning reveals their functions at the primary cilium. *PLoS Biol* **18**, e3000679 (2020).
13. Gheiratmand, L. *et al.* Spatial and proteomic profiling reveals centrosome-independent features of centriolar satellites. *EMBO J* 38, e101109 (2019).
14. Gupta, G.D. *et al.* A Dynamic Protein Interaction Landscape of the Human Centrosome-Cilium Interface. *Cell* **163**, 1484-1499 (2015).
15. Quarantotti, V. *et al.* Centriolar satellites are acentriolar assemblies of centrosomal proteins. *EMBO J* 38, e101082 (2019).
16. Joachim, J. *et al.* Centriolar Satellites Control GABARAP Ubiquitination and GABARAP-Mediated Autophagy. *Curr Biol* **27**, 2123-2136 e2127 (2017).
17. Lopes, C.A. *et al.* Centriolar satellites are assembly points for proteins implicated in human ciliopathies, including oral-facial-digital syndrome 1. *J Cell Sci* **124**, 600-612 (2011).
18. Odabasi, E., Batman, U. & Firat-Karalar, E.N. Unraveling the mysteries of centriolar satellites: time to rewrite the textbooks about the centrosome/cilium complex. *Mol Biol Cell* **31**, 866-872 (2020).

19. Prosser, S.L. & Pelletier, L. Centriolar satellite biogenesis and function in vertebrate cells. *J Cell Sci* **133,** jcs239566 (2020).
20. Tischer, J., Carden, S. & Gergely, F. Accessorizing the centrosome: new insights into centriolar appendages and satellites. *Curr Opin Struct Biol* **66**, 148-155 (2021).
21. Abal, M., Keryer, G. & Bornens, M. Centrioles resist forces applied on centrosomes during G2/M transition. *Biol Cell* **97**, 425-434 (2005).
22. Ge, X., Frank, C.L., Calderon de Anda, F. & Tsai, L.H. Hook3 interacts with PCM1 to regulate pericentriolar material assembly and the timing of neurogenesis. *Neuron* **65**, 191-203 (2010).
23. Monroe, T.O. *et al.* PCM1 is necessary for focal ciliary integrity and is a candidate for severe schizophrenia. *Nat Commun* **11**, 5903 (2020).
24. Prosser, S.L. *et al.* Aggresome assembly at the centrosome is driven by CP110-CEP97-CEP290 and centriolar satellites. *Nat Cell Biol* **24**, 483-496 (2022).
25. Stowe, T.R., Wilkinson, C.J., Iqbal, A. & Stearns, T. The centriolar satellite proteins Cep72 and Cep290 interact and are required for recruitment of BBS proteins to the cilium. *Mol Biol Cell* **23**, 3322-3335 (2012).
26. Villumsen, B.H. *et al.* A new cellular stress response that triggers centriolar satellite reorganization and ciliogenesis. *EMBO J* **32**, 3029-3040 (2013).
27. Zhao, H. *et al.* Fibrogranular materials function as organizers to ensure the fidelity of multiciliary assembly. *Nat Commun* **12**, 1273 (2021).
28. Zoubovsky, S. *et al.* Neuroanatomical and behavioral deficits in mice haploinsufficient for Pericentriolar material 1 (Pcm1). *Neurosci Res* **98**, 45-49 (2015).
29. Kubo, A. & Tsukita, S. Non-membranous granular organelle consisting of PCM-1: subcellular distribution and cell-cycle-dependent assembly/disassembly. *J Cell Sci* **116**, 919-928 (2003).
30. So, C. *et al.* A liquid-like spindle domain promotes acentrosomal spindle assembly in mammalian oocytes. *Science* **364, eaaw2166** (2019).
31. Srsen, V., Fant, X., Heald, R., Rabouille, C. & Merdes, A. Centrosome proteins form an insoluble perinuclear matrix during muscle cell differentiation. *BMC Cell Biol* **10**, 28 (2009).
32. Viggars, M.R. *et al.* PCM1 labeling reveals myonuclear and nuclear dynamics in skeletal muscle across species. *Am J Physiol Cell Physiol* **324**, C85-C97 (2023).
33. Nachury, M.V. *et al.* A core complex of BBS proteins cooperates with the GTPase Rab8 to promote ciliary membrane biogenesis. *Cell* **129**, 1201-1213 (2007).
34. Odabasi, E. *et al.* CCDC66 regulates primary cilium length and signaling via interactions with transition zone and axonemal proteins. *J Cell Sci* **136, jcs260327** (2023).
35. Tollenaere, M.A.X. *et al.* p38- and MK2-dependent signalling promotes stress-induced centriolar satellite remodelling via 14-3-3-dependent sequestration of CEP131/AZI1. *Nat Commun* **6**, 10075 (2015).
36. Firat-Karalar, E.N., Rauniyar, N., Yates, J.R., 3rd & Stearns, T. Proximity interactions among centrosome components identify regulators of centriole duplication. *Curr Biol* **24**, 664-670 (2014).

37. Conkar, D., Bayraktar, H. & Firat-Karalar, E.N. Centrosomal and ciliary targeting of CCDC66 requires cooperative action of centriolar satellites, microtubules and molecular motors. *Sci Rep* **9**, 14250 (2019).
38. Rai, A.K., Chen, J.X., Selbach, M. & Pelkmans, L. Kinase-controlled phase transition of membraneless organelles in mitosis. *Nature* **559**, 211-216 (2018).
39. Pachinger, C. *et al.* A conserved role for centriolar satellites in translation of centrosomal and ciliary proteins. J Cell Biol 224, e202408042 (2025).
40. Kroschwald, S. *et al.* Promiscuous interactions and protein disaggregases determine the material state of stress-inducible RNP granules. *Elife* **4**, e06807 (2015).
41. Wheeler, J.R., Matheny, T., Jain, S., Abrisch, R. & Parker, R. Distinct stages in stress granule assembly and disassembly. *Elife* **5, e18413** (2016).
42. Geiger, T. *et al.* Initial quantitative proteomic map of 28 mouse tissues using the SILAC mouse. *Mol Cell Proteomics* **12**, 1709-1722 (2013).
43. Hein, M.Y. *et al.* A human interactome in three quantitative dimensions organized by stoichiometries and abundances. *Cell* **163**, 712-723 (2015).
44. Wang, M., Herrmann, C.J., Simonovic, M., Szklarczyk, D. & von Mering, C. Version 4.0 of PaxDb: Protein abundance data, integrated across model organisms, tissues, and cell-lines. *Proteomics* **15**, 3163-3168 (2015).
45. Erdos, G. & Dosztanyi, Z. AIUPred: combining energy estimation with deep learning for the enhanced prediction of protein disorder. *Nucleic Acids Res* **52**, W176-W181 (2024).
46. Joachim, J. *et al.* Activation of ULK Kinase and Autophagy by GABARAP Trafficking from the Centrosome Is Regulated by WAC and GM130. *Mol Cell* **60**, 899-913 (2015).
47. Wang, J. *et al.* The conserved domain database in 2023. *Nucleic Acids Res* **51**, D384-D388 (2023).
48. Wirth, M. *et al.* Molecular determinants regulating selective binding of autophagy adapters and receptors to ATG8 proteins. *Nat Commun* **10**, 2055 (2019).
49. Jiang, X. *et al.* Condensation of pericentrin proteins in human cells illuminates phase separation in centrosome assembly. *J Cell Sci* **134, jcs258876** (2021).
50. Inobe, T. & Nukina, N. Rapamycin-induced oligomer formation system of FRB-FKBP fusion proteins. *J Biosci Bioeng* **122**, 40-46 (2016).
51. Rollins, C.T. *et al.* A ligand-reversible dimerization system for controlling protein-protein interactions. *Proc Natl Acad Sci U S A* **97**, 7096-7101 (2000).
52. Bose, M., Lampe, M., Mahamid, J. & Ephrussi, A. Liquid-to-solid phase transition of oskar ribonucleoprotein granules is essential for their function in Drosophila embryonic development. *Cell* **185**, 1308-1324 e1323 (2022).
53. Patel, A. *et al.* A Liquid-to-Solid Phase Transition of the ALS Protein FUS Accelerated by Disease Mutation. *Cell* **162**, 1066-1077 (2015).
54. Chevrier, V. *et al.* OFIP/KIAA0753 forms a complex with OFD1 and FOR20 at pericentriolar satellites and centrosomes and is mutated in one individual with oral-facial-digital syndrome. *Hum Mol Genet* **25**, 497-513 (2016).
55. Kim, J., Krishnaswami, S.R. & Gleeson, J.G. CEP290 interacts with the centriolar satellite component PCM-1 and is required for Rab8 localization to the primary cilium. *Hum Mol Genet* **17**, 3796-3805 (2008).

56. Kim, K., Lee, K. & Rhee, K. CEP90 is required for the assembly and centrosomal accumulation of centriolar satellites, which is essential for primary cilia formation. *PLoS One* **7**, e48196 (2012).
57. Kobayashi, T., Kim, S., Lin, Y.C., Inoue, T. & Dynlacht, B.D. The CP110-interacting proteins Talpid3 and Cep290 play overlapping and distinct roles in cilia assembly. *J Cell Biol* **204**, 215-229 (2014).
58. Kodani, A. *et al.* Centriolar satellites assemble centrosomal microcephaly proteins to recruit CDK2 and promote centriole duplication. *Elife* **4, e07438** (2015).
59. Tozer, S., Baek, C., Fischer, E., Goiame, R. & Morin, X. Differential Routing of Mindbomb1 via Centriolar Satellites Regulates Asymmetric Divisions of Neural Progenitors. *Neuron* **93**, 542-551 e544 (2017).
60. Kim, J.C. *et al.* The Bardet-Biedl protein BBS4 targets cargo to the pericentriolar region and is required for microtubule anchoring and cell cycle progression. *Nat Genet* **36**, 462-470 (2004).
61. Mennella, V. *et al.* Subdiffraction-resolution fluorescence microscopy reveals a domain of the centrosome critical for pericentriolar material organization. *Nat Cell Biol* **14**, 1159-1168 (2012).
62. Sonnen, K.F., Schermelleh, L., Leonhardt, H. & Nigg, E.A. 3D-structured illumination microscopy provides novel insight into architecture of human centrosomes. *Biol Open* **1**, 965-976 (2012).
63. West, J.A. *et al.* Structural, super-resolution microscopy analysis of paraspeckle nuclear body organization. *J Cell Biol* **214**, 817-830 (2016).
64. Frikstad, K.M. *et al.* A CEP104-CSPP1 Complex Is Required for Formation of Primary Cilia Competent in Hedgehog Signaling. *Cell Rep* **28**, 1907-1922 e1906 (2019).
65. Goncalves, J. & Pelletier, L. The Ciliary Transition Zone: Finding the Pieces and Assembling the Gate. *Mol Cells* **40**, 243-253 (2017).
66. Drivas, T.G. & Bennett, J. CEP290 and the primary cilium. *Adv Exp Med Biol* **801**, 519-525 (2014).
67. Travaglini, L. *et al.* Expanding CEP290 mutational spectrum in ciliopathies. *Am J Med Genet A* **149A**, 2173-2180 (2009).
68. Firat-Karalar, E.N. The ciliopathy gene product Cep290 is required for primary cilium formation and microtubule network organization. *Turk J Biol* **42**, 371-381 (2018).
69. Yu, N. *et al.* Isolation of Functional Tubulin Dimers and of Tubulin-Associated Proteins from Mammalian Cells. *Curr Biol* **26**, 1728-1736 (2016).
70. Guillen-Boixet, J. *et al.* RNA-Induced Conformational Switching and Clustering of G3BP Drive Stress Granule Assembly by Condensation. *Cell* **181**, 346-361 e317 (2020).
71. Sanders, D.W. *et al.* Competing Protein-RNA Interaction Networks Control Multiphase Intracellular Organization. *Cell* **181**, 306-324 e328 (2020).
72. Yang, P. *et al.* G3BP1 Is a Tunable Switch that Triggers Phase Separation to Assemble Stress Granules. *Cell* **181**, 325-345 e328 (2020).
73. Prasai, A. *et al.* The BBSome assembly is spatially controlled by BBS1 and BBS4 in human cells. *J Biol Chem* **295**, 14279-14290 (2020).

74. Tian, X., Zhao, H. & Zhou, J. Organization, functions, and mechanisms of the BBSome in development, ciliopathies, and beyond. *Elife* **12, e85723** (2023).
75. Hu, S. *et al.* Time-resolved proteomic profiling reveals compositional and functional transitions across the stress granule life cycle. *Nat Commun* **14**, 7782 (2023).
76. Marmor-Kollet, H. *et al.* Spatiotemporal Proteomic Analysis of Stress Granule Disassembly Using APEX Reveals Regulation by SUMOylation and Links to ALS Pathogenesis. *Mol Cell* **80**, 876-891 e876 (2020).
77. Fare, C.M., Villani, A., Drake, L.E. & Shorter, J. Higher-order organization of biomolecular condensates. *Open Biol* **11**, 210137 (2021).
78. Jain, S. *et al.* ATPase-Modulated Stress Granules Contain a Diverse Proteome and Substructure. *Cell* **164**, 487-498 (2016).
79. Lallemand-Breitenbach, V. & de The, H. PML nuclear bodies: from architecture to function. *Curr Opin Cell Biol* **52**, 154-161 (2018).
80. Luders, J. The amorphous pericentriolar cloud takes shape. *Nat Cell Biol* **14**, 1126-1128 (2012).
81. Youn, J.Y. *et al.* High-Density Proximity Mapping Reveals the Subcellular Organization of mRNA-Associated Granules and Bodies. *Mol Cell* **69**, 517-532 e511 (2018).
82. Yu, F. *et al.* O-GlcNAcylation Regulates Centrosome Behavior and Cell Polarity to Reduce Pulmonary Fibrosis and Maintain the Epithelial Phenotype. *Adv Sci (Weinh)* **10**, e2303545 (2023).
83. Hori, A., Barnouin, K., Snijders, A.P. & Toda, T. A non-canonical function of Plk4 in centriolar satellite integrity and ciliogenesis through PCM1 phosphorylation. *EMBO Rep* **17**, 326-337 (2016).
84. Renaud, C.C.N. & Bidere, N. Function of Centriolar Satellites and Regulation by Post-Translational Modifications. *Front Cell Dev Biol* **9**, 780502 (2021).
85. Ehrentraut, S. *et al.* t(8;9)(p22;p24)/PCM1-JAK2 activates SOCS2 and SOCS3 via STAT5. *PLoS One* **8**, e53767 (2013).
86. Gurling, H.M. *et al.* Genetic association and brain morphology studies and the chromosome 8p22 pericentriolar material 1 (PCM1) gene in susceptibility to schizophrenia. *Arch Gen Psychiatry* **63**, 844-854 (2006).
87. Hoeller, S., Walz, C., Reiter, A., Dirnhofer, S. & Tzankov, A. PCM1-JAK2-fusion: a potential treatment target in myelodysplastic-myeloproliferative and other hemato-lymphoid neoplasms. *Expert Opin Ther Targets* **15**, 53-62 (2011).
88. Kamiya, A. *et al.* Recruitment of PCM1 to the centrosome by the cooperative action of DISC1 and BBS4: a candidate for psychiatric illnesses. *Arch Gen Psychiatry* **65**, 996-1006 (2008).
89. Masselli, E. *et al.* Implication of MAPK1/MAPK3 signalling pathway in t(8;9)(p22;24)/PCM1-JAK2 myelodysplastic/myeloproliferative neoplasms. *Br J Haematol* **162**, 563-566 (2013).
90. Patterer, V., Schnittger, S., Kern, W., Haferlach, T. & Haferlach, C. Hematologic malignancies with PCM1-JAK2 gene fusion share characteristics with myeloid and lymphoid neoplasms with eosinophilia and abnormalities of PDGFRA, PDGFRB, and FGFR1. *Ann Hematol* **92**, 759-769 (2013).

91. Mohapatra, S. & Wegmann, S. Biomolecular condensation involving the cytoskeleton. *Brain Res Bull* **194**, 105-117 (2023).
92. Volkov, V.A. & Akhmanova, A. Phase separation on microtubules: from droplet formation to cellular function? *Trends Cell Biol* **34**, 18-30 (2024).
93. Gurkaslar, H.K., Culfa, E., Arslanhan, M.D., Lince-Faria, M. & Firat-Karalar, E.N. CCDC57 Cooperates with Microtubules and Microcephaly Protein CEP63 and Regulates Centriole Duplication and Mitotic Progression. *Cell Rep* **31**, 107630 (2020).
94. Arslanhan, M.D. *et al.* CCDC15 localizes to the centriole inner scaffold and controls centriole length and integrity. *J Cell Biol* **222** (2023).
95. Sprague, B.L., Pego, R.L., Stavreva, D.A. & McNally, J.G. Analysis of binding reactions by fluorescence recovery after photobleaching. *Biophys J* **86**, 3473-3495 (2004).
96. Hughes, C.S. *et al.* Ultrasensitive proteome analysis using paramagnetic bead technology. *Mol Syst Biol* **10**, 757 (2014).
97. Moggridge, S., Sorensen, P.H., Morin, G.B. & Hughes, C.S. Extending the Compatibility of the SP3 Paramagnetic Bead Processing Approach for Proteomics. *J Proteome Res* **17**, 1730-1740 (2018).
98. Werner, T. *et al.* Ion coalescence of neutron encoded TMT 10-plex reporter ions. *Anal Chem* **86**, 3594-3601 (2014).
99. Ritchie, M.E. *et al.* limma powers differential expression analyses for RNA-sequencing and microarray studies. *Nucleic Acids Res* **43**, e47 (2015).

Figure 1

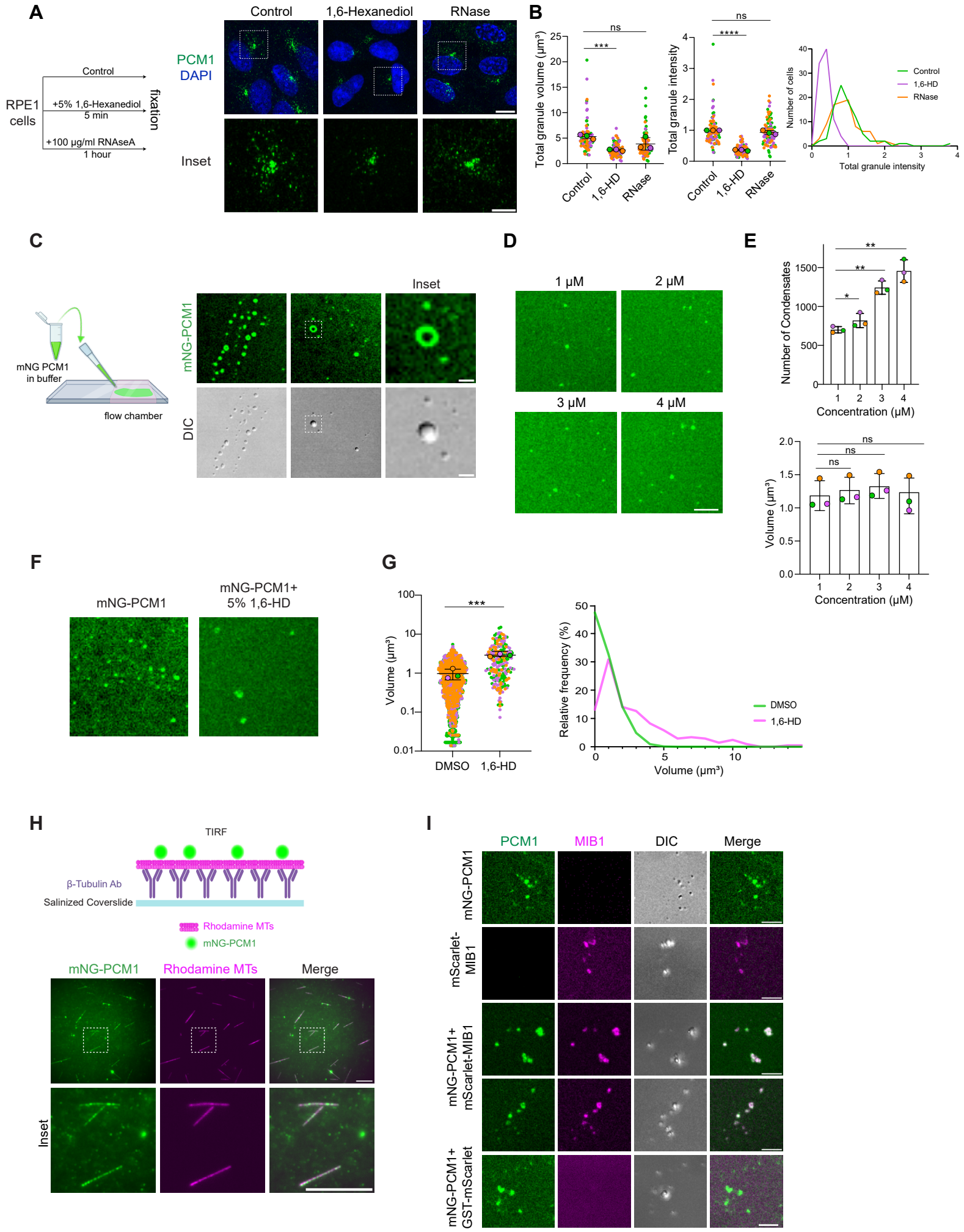
A
Control
1,6-Hexanediol
RNase
RPE1 cells
Control
+5% 1,6-Hexanediol
5 min
+100 µg/ml RNAseA
1 hour
fixation
PCM1
DAPI
Inset
B
Total granule volume (µm³)
Total granule intensity
Number of cells
Control
1,6-HD
RNase
ns
***
****
C
mNG PCM1 in buffer
flow chamber
mNG-PCM1
DIC
Inset
D
1 µM
2 µM
3 µM
4 µM
E
Number of Condensates
Concentration (µM)
Volume (µm³)
ns
*
**
F
mNG-PCM1
mNG-PCM1+ 5% 1,6-HD
G
Volume (µm³)
DMSO
1,6-HD
Relative frequency (%)
H
TIRF
β-Tubulin Ab
Salinized Coverslide
Rhodamine MTs
mNG-PCM1
mNG-PCM1
Rhodamine MTs
Merge
Inset
I
PCM1
MIB1
DIC
Merge
mNG-PCM1
mScarlet-MIB1
mNG-PCM1+ mScarlet-MIB1
mNG-PCM1+ GST-mScarlet

Figure 1

Roles of RNA and multivalent interactions on CS maintenance.

(A) Representative confocal images of RPE1 cells treated with different reagents, fixed with methanol and stained with anti-PCM1-C Ab and DAPI for nucleus. Untreated cells serve as the control. Cells were treated with 5% 1,6-hexanediol for 5 minutes, 100 µg/ml RNase A+I for 1 hour. Scale bars: 10 µm (main panels), 5 µm (insets).

(B) Total volume of granules per cell (μm^3) and total granule intensity values were measured using Imaris software. Granule intensity was normalized to control values for each replicate. Number of cells for each total intensity value was determined from relative frequency data. Statistical significance was determined by the Student's *t*-test (paired and two-tailed). Results are from three biological replicates, green, magenta and orange colored dots representing different replicates. n=30 cells for each replicate. *P<0.05; **P<0.01, ***P<0.001****P<0.0001; ns, not significant.

PCM1 exhibits intrinsic properties for granule formation, client sequestration, and microtubule binding *in vitro.*

(C) Schematic depicts the experimental flow. mNeonGreen-PCM1 condensates in a phase separation buffer at 1 µM, flown in chambers and imaged using a confocal microscope. Scale bar, 2 µm for field of view.

(D) mNeonGreen-PCM1 condensates in phase separation buffer at concentrations 1, 2, 3, 4 µM.

(E) Quantification of the number of condensates in the phase separation buffer from D. Results are from three biological replicates.

(F) Representative images of mNeonGreen-PCM1 condensates treated with 1,6-hexanediol. mNeonGreen-PCM1 condensates in phase separation buffer at 1 mM protein concentration upon 1,6-hexanediol treatment were set, flown in chambers and imaged. Scale bar, 5 µm.

(G) Quantification of the number of condensates in the phase separation buffer from F. Results are from three biological replicates, green, magenta and orange colored dots representing different replicates. Relative frequency percentage of granule volumes were calculated for each granule for DMSO and 1,6-HD treatment, in green and magenta respectively.

(H) Schematic depicts the experimental flow. Taxol stabilized microtubules polymerized from purified bovine tubulin labeled with Alexa Fluor 568 were attached on salinized and tubulin antibody coated cover slide surface. mNeonGreen-PCM1 was

flown in a chamber and imaged with TIRF microscopy. Scale bar, 10 μm (main panels); 2 μm (insets).

(I) mNeonGreen-PCM1, mScarlet-MIB1 and GST-mScarlet were set individually and combined in phase separation buffer, flown in chambers and imaged. Scale bar, 5 μm.

Figure 2

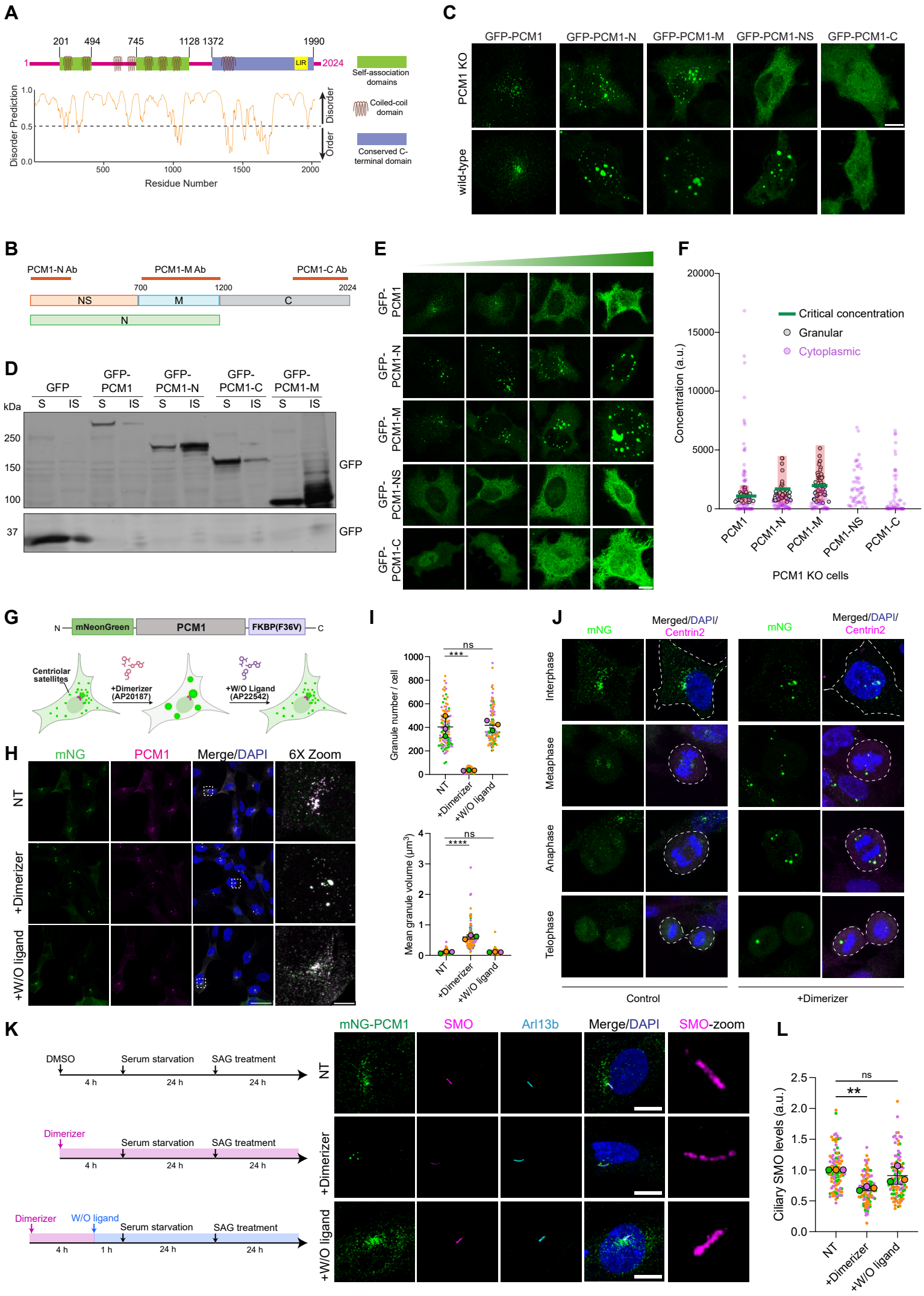
A
201
494
745
1128 1372
1990
1
LIR
2024
Self-association domains
Coiled-coil domain
Conserved C-terminal domain
Disorder Prediction
1.0
0.5
0.0
Disorder
Order
500
1000
1500
2000
Residue Number
B
PCM1-N Ab
PCM1-M Ab
PCM1-C Ab
700
1200
2024
NS
M
C
N
C
GFP-PCM1
GFP-PCM1-N
GFP-PCM1-M
GFP-PCM1-NS
GFP-PCM1-C
PCM1 KO
wild-type
D
GFP
GFP-PCM1
GFP-PCM1-N
GFP-PCM1-C
GFP-PCM1-M
S
IS
kDa
250
150
100
37
GFP
GFP
E
GFP-PCM1
GFP-PCM1-N
GFP-PCM1-M
GFP-PCM1-NS
GFP-PCM1-C
F
20000
15000
10000
5000
0
Concentration (a.u.)
Critical concentration
Granular
Cytoplasmic
PCM1
PCM1-N
PCM1-M
PCM1-NS
PCM1-C
PCM1 KO cells
G
N
mNeonGreen
PCM1
FKBP(F36V)
C
Centriolar satellites
+Dimerizer (AP20187)
+W/O Ligand (AP22542)
H
mNG
PCM1
Merge/DAPI
6X Zoom
NT
+Dimerizer
+W/O ligand
I
ns
***
1000
800
600
400
200
0
Granule number / cell
NT
+Dimerizer
+W/O ligand
ns
****
4
3
2
1
0
Mean granule volume (μm³)
NT
+Dimerizer
+W/O ligand
J
mNG
Merged/DAPI/Centrin2
mNG
Merged/DAPI/Centrin2
Interphase
Metaphase
Anaphase
Telophase
Control
+Dimerizer
K
DMSO
Serum starvation
SAG treatment
4 h
24 h
24 h
Dimerizer
Serum starvation
SAG treatment
4 h
24 h
24 h
Dimerizer
W/O ligand
Serum starvation
SAG treatment
4 h
1 h
24 h
24 h
mNG-PCM1
SMO
Arl13b
Merge/DAPI
SMO-zoom
NT
+Dimerizer
+W/O ligand
L
ns
**
2.5
2.0
1.5
1.0
0.5
0.0
Ciliary SMO levels (a.u.)
NT
+Dimerizer
+W/O ligand

Figure 2

PCM1 is a modular protein with domains important for granule formation and regulation of granule properties.

(A) Schematic representation of the domain architecture of human PCM1. The *PCM1* gene encodes a 2024 amino acid (aa) acidic protein with a molecular weight of 228 kDa and an isoelectric point (pI) of 4.99. It contains 8 coiled-coil domains, each represented by gray coils located at CC1: 270–293 aa, CC2: 493–513 aa, CC3: 652–682 aa, CC4: 732–769 aa, CC5: 826–853 aa, CC6: 989–1016 aa, CC7: 1065–1085 aa, and CC8: 1517–1537 aa. It is highly enriched in intrinsically disordered regions (IDRs) predicted by PONDR (predictor of naturally disordered regions) with the VL3 model. Scores above 0.5 indicate disordered regions, whereas scores below 0.5 are ordered. PCM1 contains two self-association domains (201–494 aa and 745–1128 aa, in green), a conserved C-terminal domain (1372–1990 aa, in blue), and an LC3-interacting region (LIR) domain (1953–1958, in yellow).

(B) Schematic representation of PCM1 truncation constructs designed based on domain analysis and the presence or absence of self-association domains. PCM1-NS contains the first self-association domain, PCM1-M contains the second, and PCM1-N includes both, whereas PCM1-C lacks them. Three antibodies targeting PCM1 at different regions are shown in red (PCM1-N-Ab targets 1-254 aa, PCM1-M-Ab targets 700-1200 aa, PCM1-C-Ab targets 1664-2024 aa).

(C) PCM1 truncation mutants and their subcellular localization. Representative confocal images show HeLa-WT and HeLa::PCM1 KO cells transfected with the indicated constructs. Cells were stained for anti-GFP. Similar results were obtained from three biological replicates. Scale bar: 10 μm.

(D) Solubility analysis of GFP-PCM1 and truncation mutants. Immunoblot analysis of lysates from HEK293T cells transfected with GFP, GFP-PCM1, GFP-PCM1-N, GFP-PCM1-C, and GFP-PCM1-M plasmids for 48 hours. Cells were lysed with pulldown buffer and separated as the soluble fraction (S). Remaining insoluble fraction was further lysed with 2X sample buffer. Membranes were stained with anti-GFP-Ab. S: Soluble, IS: Insoluble.

(E) Localization of PCM1 and its truncation mutants at increasing concentrations in HeLa::PCM1 KO cells. These cells are transfected with GFP fusions of PCM1, PCM1-N, PCM1-M, PCM1-NS and PCM1-C for 48 hours, fixed and stained with anti-GFP. The images indicate the cells with increasing expression levels of PCM1 and its truncations, indicated by a green triangle at the top. Scale bar: 10 μm.

(F) Quantification of critical saturation concentrations (Csat) of PCM1 and its truncations from (E). For each transfected cell, intensity of GFP signal and total volume and intensity of granules and cytoplasm were measured using Imaris

Software. Critical concentration denotes the mean value of granular concentration values. Results are from three biological replicates, min 48 cells in total. a.u.: arbitrary unit.

(G) Schematic representation and validation of the chemically inducible CS dimerization system. mNeonGreen-PCM1 is fused to the FKBP(F36V) mutant, which dimerizes upon the addition of AP20187 (homodimerizer) and dimerization is reversed with AP22542 (wash-out ligand) treatment.

(H) Chemically inducible homodimerization of PCM1 alters CS granule properties. The images represent CS granules under three conditions in RPE1::PCM1 KO cells stably expressing mNG-PCM1-FKBP(F36V): no treatment (NT), with the dimerizer, and with the wash-out (W/O) ligand after dimerization. Cells were treated with the dimerizer for 4 hours and then either fixed directly or treated with the wash-out ligand for 1 hour before fixation. Cells were stained with antibodies for mNeonGreen and PCM1. Scale bars: 30 μm (main panels), 5 μm (insets)

(I) Quantification of CS granule properties from (H). Granule number per cell and mean granule volume were quantified using Imaris Software. Results are from three biological replicates, green, magenta and orange colored dots representing different replicates. n=35 cells for each replicate.

(J) Characterization of CS granules following inducible dimerization at various stages of mitosis. Cells were fixed and stained for mNeonGreen and Centrin 2. Representative images show CS granules in control and dimerizer-treated cells at interphase, metaphase, anaphase, and telophase. Scale bar: 10 μm.

(K) The effect of disrupting CS granule properties on ciliary signaling. The images represent CS granules under three conditions in RPE1::PCM1 KO cells stably expressing mNG-PCM1-FKBP(F36V): no treatment (NT), with the dimerizer, and with the wash-out (W/O) ligand after dimerization. Ciliation was induced by serum starvation for 24 hours. The Sonic Hedgehog pathway was activated by treating cells with 50 nM of the Smoothened agonist SAG for 24 hours. Cells were fixed and stained for mNeonGreen, SMO, and Arl13b. Scale bars: 20 μm (main panels), 5 μm (insets)

(L) Quantification of Smo recruitment to the cilium as shown in (K). Smo intensity at the cilium was calculated using ImageJ. Only mNG-PCM1-positive cells were selected for quantification. The data represent the mean from three biological replicates, green, magenta and orange colored dots representing different replicates. ns: not significant.

Figure 3

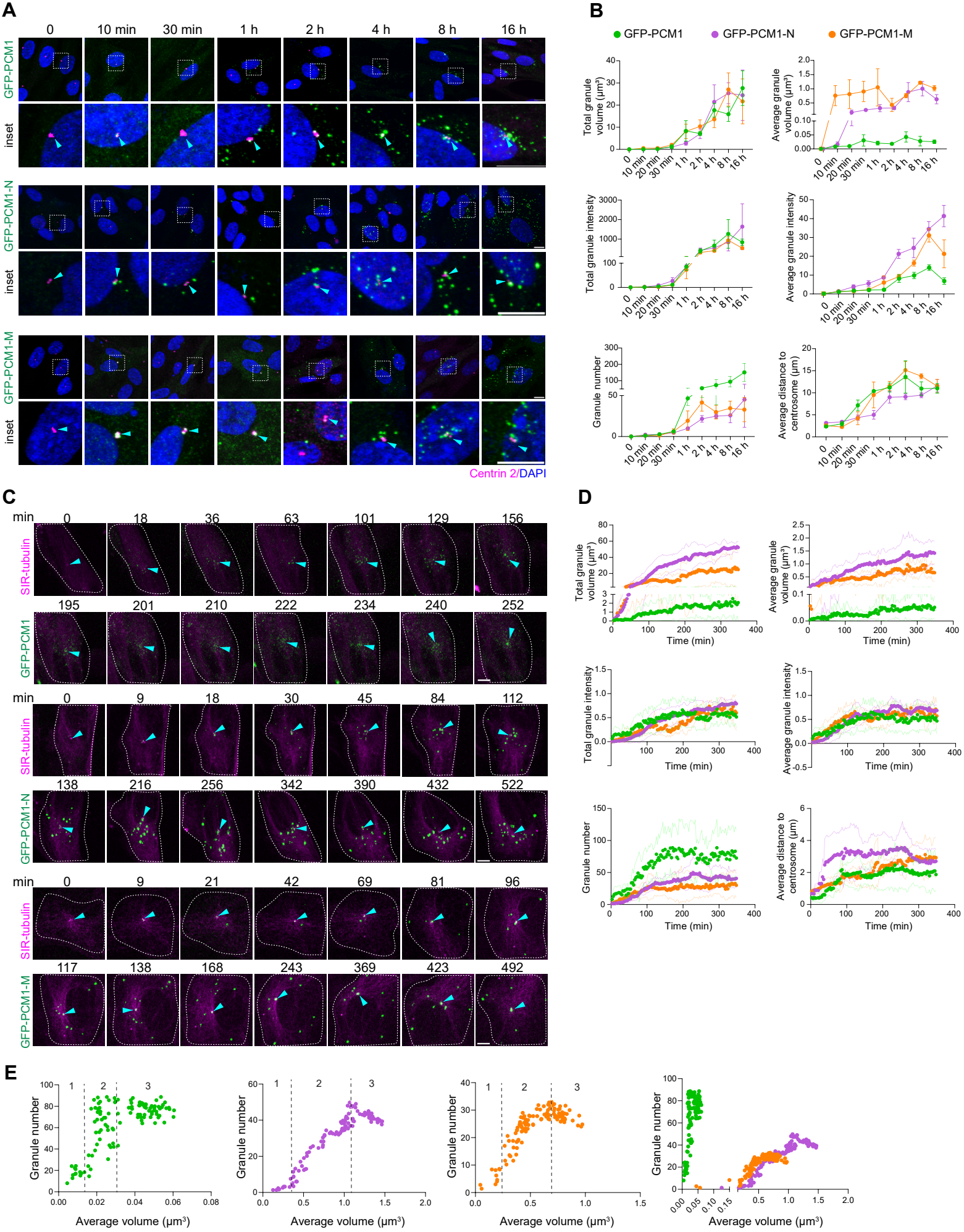
A
0
10 min
30 min
1 h
2 h
4 h
8 h
16 h
GFP-PCM1
inset
GFP-PCM1-N
inset
GFP-PCM1-M
inset
Centrin 2/DAPI
B
GFP-PCM1
GFP-PCM1-N
GFP-PCM1-M
Total granule volume (µm³)
Average granule volume (µm³)
Total granule intensity
Average granule intensity
Granule number
Average distance to centrosome (µm)
C
min
SIR-tubulin
GFP-PCM1
GFP-PCM1-N
GFP-PCM1-M
D
Time (min)
E
Granule number
Average volume (µm³)

Figure 3

Spatiotemporal dynamics of PCM1 scaffold formation during CS biogenesis.

(A) Fixed imaging of cells from the *de novo* CS biogenesis assay. Representative confocal images of PCM1 granule formation in RPE1::PCM1 KO cells inducibly expressing GFP-PCM1, GFP-PCM1-N and GFP-PCM1-M. Cells were induced by 1 μM doxycycline for 10 minutes, 30 minutes, 1 hour, 2 hours, 4 hours, 8 hours or 16 hours, fixed and stained with antibodies for GFP and Centrin-2 and DAPI for nucleus. Cyan arrowhead denotes centrosomes at each time point. Scale bars: 10 μm (main panels), 2 μm (insets)

(B) Quantification of size, fluorescence intensity and number of PCM1 granules from (A). Total volume of granules per cell (μm^3), average volume of granules per cell (μm^3), total granule intensity, average granule intensity, granule number, and average distance of granules to centrosome (μm) values were measured using Imaris software. Average values represent total values divided by the number of granules for each cell. Average distance to centrosome values were quantified from the distance between granules and centrosomes marked by centrin 2 for each cell. Results are from three biological replicates, n=48 cells per time point.

(C) Time-lapse confocal imaging of PCM1 granules from the *de novo* CS biogenesis assay. Images represent still frames from time-lapse confocal images of RPE1::PCM1 KO cells inducibly expressing GFP-PCM1, GFP-PCM1-N, and GFP-PCM1-M. Cells were imaged following the addition of 1 μM doxycycline and SIR-tubulin. The time labeled '0 min' marks the initiation of granule nucleation. Centrosomes are indicated by cyan arrowheads at each time point, and cell boundaries are outlined with white dashed lines. Frame times (in minutes) are displayed at the top of each image. Scale bars: 5 μm.

(D) Quantification of size, fluorescence intensity and number of PCM1 granules from C as described in (B). Average distance to centrosome values were quantified from the distance between granules and SIR-tubulin staining for each cell. Images were taken in 3 minute intervals for 348 minutes. Results are from three biological replicates, data represents the mean of n=5 cells.

(E) Relationship between average PCM1 granule volume and number during *de novo* CS biogenesis. The average granule volume per cell (μm^3) and the number of granules were quantified using Imaris software. Results are from three biological replicates, n=5 cells analyzed.. Assembly progression is categorized into three phases: (1) nucleation, (2) growth, and (3) steady-state."

Figure 4

A

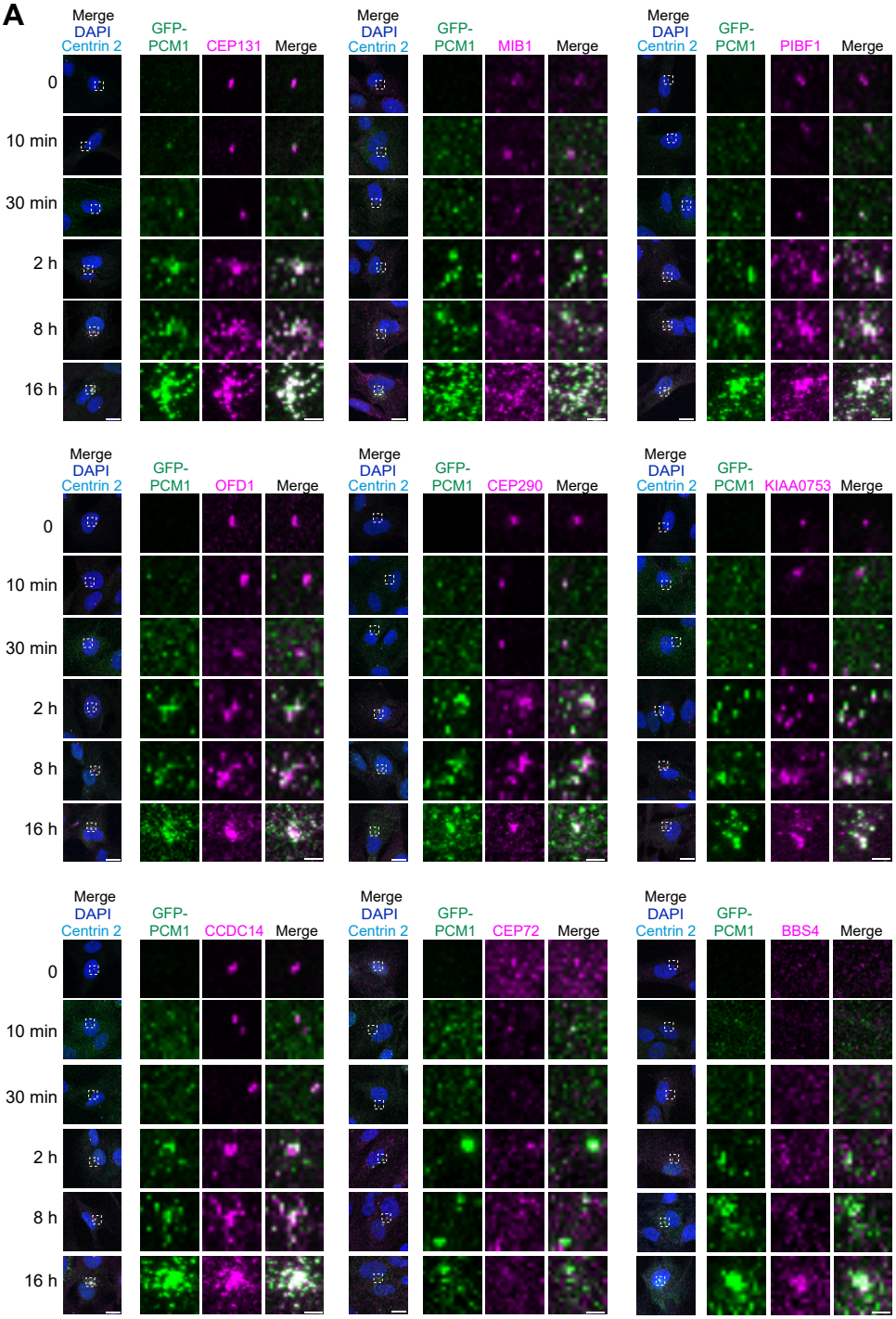

B

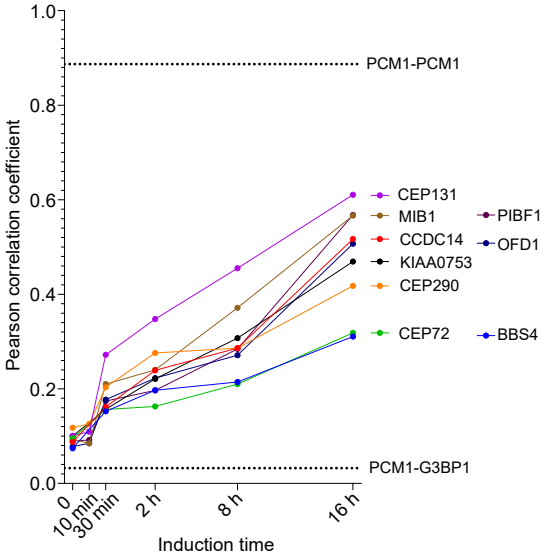

C

	10 min	30 min	2 h	8 h	16 h
BBS4	-	-	+	+	+++
CCDC14	-	-	+	++	++++
CEP72	-	-	-	+	++
CEP131	-	+	++	+++	++++
CEP290	-	-	+	+	+++
KIAA0753	-	-	+	++	+++
MIB1	-	+	+	+++	++++
OFD1	-	+	+	++	++++
PIBF1	-	-	+	++	++++

+: 2X ++: 3X +++: 3.5X ++++: 5X

Figure 4

Spatiotemporal analysis of client recruitment during CS biogenesis.

(A) RPE1::PCM1 KO cells inducibly expressing GFP-PCM1 were fixed before induction and 10 min, 30 min, 2 hours, 8 hours, 16 hours after induction. They were then stained with antibodies for GFP and clients denoted in magenta. Representative confocal images are shown for each client and time point. White dashed boxes highlight zoomed-in regions. Scale bars: 10 µm (main panels), 2 µm (insets)

(B) Pearson correlation coefficient (PCC) analysis of client-scaffold colocalization. PCCs between PCM1 and client proteins were calculated from 3D images using Imaris Software (intensity/voxel-based). They represent colocalization analysis across 30 cells per condition in two independent experiments. The negative control, represented by the PCC between PCM1 and G3BP1 (0.032), indicates the lower detection limit of our colocalization. The positive control, between PCM1 and PCM1 (0.887), represents the upper limit of our colocalization detection.

(C) Classification of client recruitment dynamics based on colocalization strength. Recruitment time of each client to scaffold PCM1 was determined by comparing Pearson Correlation Coefficient (PCC) values relative to the 0-minute condition. Colocalization strength was classified as positive if the PCC value at 10 minutes was at least twice that at 0 minutes. Classification thresholds are: '-' for less than 2-fold increase, '+' for 2-fold, '++' for 3-fold, '+++' for 3.5-fold, and '++++' for 5-fold increases. These thresholds were established based on the observed colocalization ranges in our dataset. A 2-fold increase marks the minimum detectable enrichment above baseline, ensuring subtle recruitment events are noted, while a 5-fold increase represents the maximum detected, with 3-fold and 3.5-fold serving as intermediate steps. This data-driven approach captures the full spectrum of recruitment behaviors effectively.

Figure 5

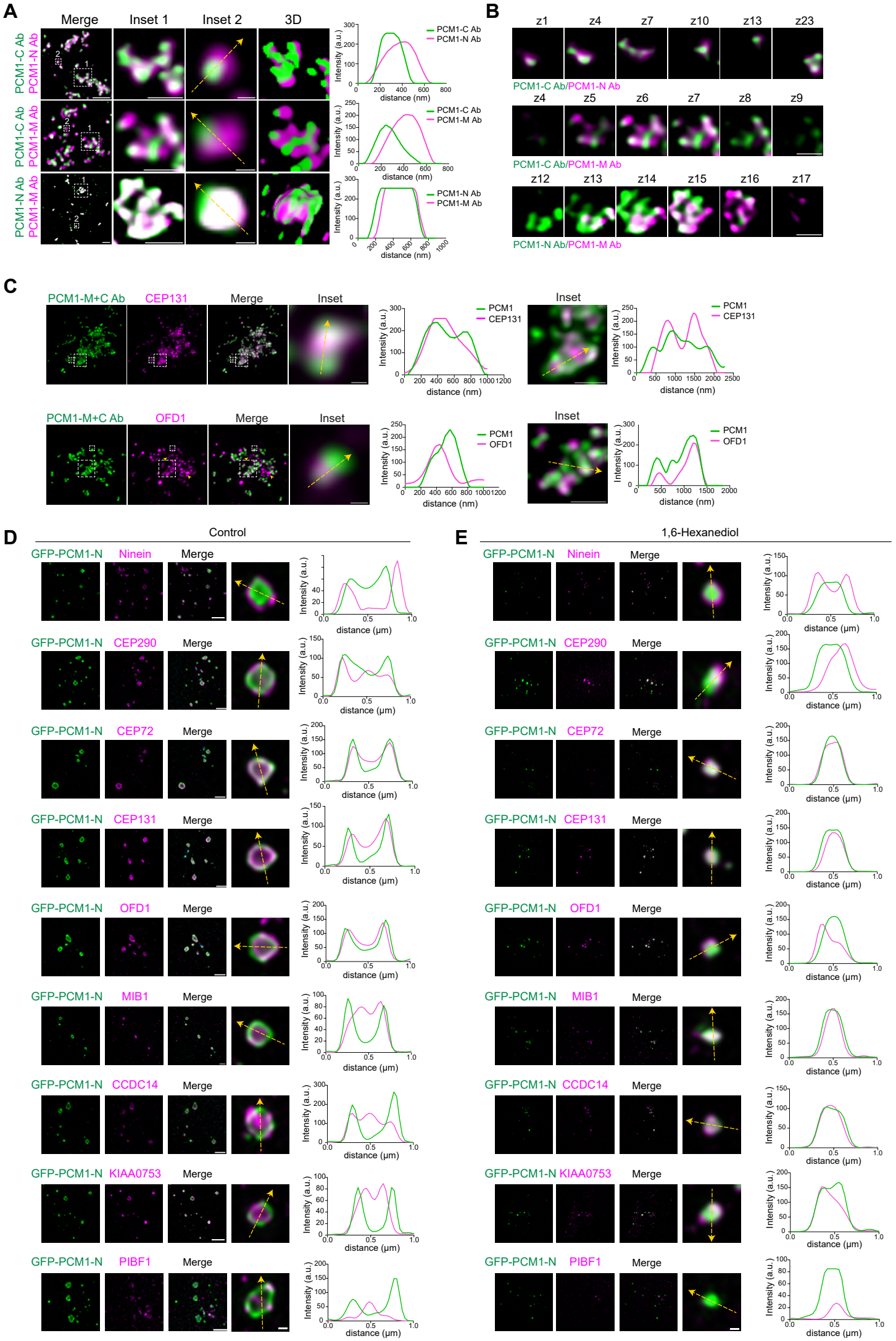
A
Merge
Inset 1
Inset 2
3D
PCM1-C Ab
PCM1-N Ab
PCM1-M Ab
Intensity (a.u.)
distance (nm)
B
z1
z4
z7
z10
z13
z23
PCM1-C Ab/PCM1-N Ab
z4
z5
z6
z7
z8
z9
PCM1-C Ab/PCM1-M Ab
z12
z13
z14
z15
z16
z17
PCM1-N Ab/PCM1-M Ab
C
PCM1-M+C Ab
CEP131
Merge
Inset
PCM1
OFD1
D
Control
GFP-PCM1-N
Ninein
CEP290
CEP72
CEP131
OFD1
MIB1
CCDC14
KIAA0753
PIBF1
distance (μm)
E
1,6-Hexanediol

Figure 5

PCM1 and clients are organized into subdomains within CS granules.

(A) Spatial organization within the PCM1 granules. RPE1 cells were processed for U-ExM and stained for combinations of PCM1-C-Ab, PCM1-M-Ab and PCM1-N-Ab in green or magenta. Scale bars shown on the images are not adjusted for the expansion factor (4.2x). Insets display 4× or 10× magnifications of the cluster or individual CS. 3D representations are rendered from Leica Software. Scale bars: 2 µm (main panels), 1 µm and 200 nm, respectively (insets).

(B) Individual Z-stack images depict the spatial organization of PCM1, as shown in (A), stained with antibodies for the PCM1-C terminus, PCM1-N terminus, and PCM1-M region.

(C) Representative confocal images of expanded CS showing the spatial organization of PCM1 and its clients. RPE1 cells were processed for U-ExM and stained for clients (green) anti-CEP131 or anti-OFD1, and anti-PCM1-M-Ab / PCM1-C-Ab mixture (magenta). Scale bars shown on the images are not adjusted for the expansion factor (4.2x). Insets display 4× or 10× magnifications of the cluster or individual CS. Arrows indicate the centrioles. Scale bars: 2 µm (main panels), 1 µm and 200 nm, respectively (insets).

(D) Spatial organization of PCM1-N and clients within CS granules. Images show high magnification of GFP-PCM1-N granules colocalizing with various client proteins. RPE1::PCM1 KO cells inducibly expressing GFP-PCM1-N were induced for 24 hours and fixed and stained with anti-GFP-Ab (green) and clients (magenta). Cells were imaged using Zeiss Elyra 7 Lattice SIM superresolution microscope. Intensity plot profiles were drawn using ImageJ. Scale bars: 0.2 µm.

(E) Spatial organization of PCM1-N and clients within CS granules after 1,6-hexanediol treatment. Images show high magnification of GFP-PCM1-N granules colocalizing with various client proteins with 1,6-hexanediol treatment. RPE1::PCM1 KO cells inducibly expressing GFP-PCM1-N were induced for 24 hours, treated with 5% 1,6-hexanediol for 5 minutes and fixed and stained with anti-GFP-Ab (green) and clients (magenta). Cells were imaged using Zeiss Elyra 7 Lattice SIM superresolution microscope. Intensity plot profiles were drawn using ImageJ. Scale bars: 0.2 µm.

Figure 6

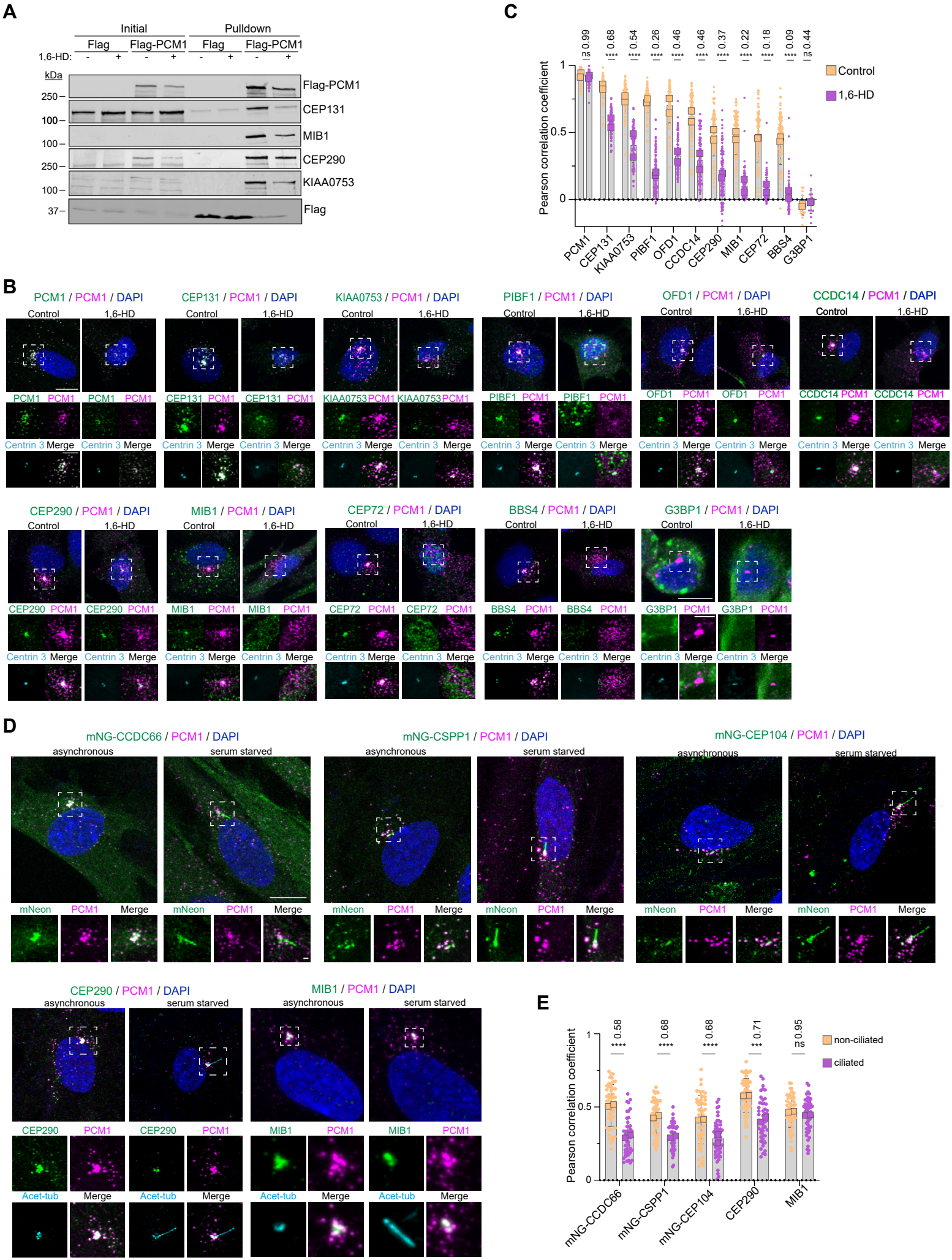
A
Initial
Pulldown
Flag
Flag-PCM1
Flag
Flag-PCM1
1,6-HD:
kDa
250
100
100
250
100
37
Flag-PCM1
CEP131
MIB1
CEP290
KIAA0753
Flag
C
Pearson correlation coefficient
Control
1,6-HD
PCM1
CEP131
KIAA0753
PIBF1
OFD1
CCDC14
CEP290
MIB1
CEP72
BBS4
G3BP1
B
PCM1 / PCM1 / DAPI
CEP131 / PCM1 / DAPI
KIAA0753 / PCM1 / DAPI
PIBF1 / PCM1 / DAPI
OFD1 / PCM1 / DAPI
CCDC14 / PCM1 / DAPI
CEP290 / PCM1 / DAPI
MIB1 / PCM1 / DAPI
CEP72 / PCM1 / DAPI
BBS4 / PCM1 / DAPI
G3BP1 / PCM1 / DAPI
Control
1,6-HD
Centrin 3
Merge
D
mNG-CCDC66 / PCM1 / DAPI
mNG-CSPP1 / PCM1 / DAPI
mNG-CEP104 / PCM1 / DAPI
asynchronous
serum starved
mNeon
PCM1
Merge
CEP290 / PCM1 / DAPI
MIB1 / PCM1 / DAPI
Acet-tub
E
Pearson correlation coefficient
non-ciliated
ciliated
mNG-CCDC66
mNG-CSPP1
mNG-CEP104
CEP290
MIB1

Figure 6

CS subdomains and granules have distinct compositions and biophysical properties

(A) Control and 1,6-hexanediol-treated HEK293T::PCM1 KO cells transfected with either FLAG or FLAG-PCM1 were lysed, and proteins were pulled down by Flag beads. The initial sample (initial) and pulled down proteins were run on an SDS gel and immunoblotted with antibodies against Flag-PCM1 and clients.

(B) RPE1 cells were treated with 5% 1,6-hexanediol for 10 min, fixed with methanol, and stained with antibodies against the indicated client proteins (green), PCM1 (magenta), centrin 3 (to mark the centrosome), and DAPI (to visualize DNA). A dual-secondary antibody labeling strategy was used to confirm PCM1 detection in both channels (top left panel). Cells in the bottom right panel were additionally treated with 50 mM sodium arsenate for 1 h to induce stress granules before 1,6-hexanediol treatment. Confocal microscopy was used for imaging. White boxes indicate zoomed-in regions. Scale bars: 10 µm (main panels), 5 µm (insets).

(C) Pearson correlation coefficient quantifying colocalization between PCM1 and client proteins. Small circles represent individual cells, while large circles indicate the average per experiment. Fold change is calculated by comparing the mean value of 1,6-hexanediol -treated samples to that of the control. Results are from two biological replicates, n = 40 cells per condition. Statistical significance was determined using a t-test comparing treatment and control for each colocalization pair (ns > 0.05, ****P < 0.0001).

(D) Asynchronous and serum starved RPE1::mNeonGreen-CCDC66, RPE1::mNeonGreen-CSPP1 and RPE1::mNeonGreen-CEP104 cells were fixed with methanol, and stained with antibodies against mNeonGreen (green) and PCM1 (magenta). Additionally, asynchronous and serum starved RPE1 cells were fixed with methanol, and stained with antibodies against the indicated client proteins (green), PCM1 (magenta) and acetylated tubulin (cyan) (to mark the primary cilia). White boxes indicate zoomed-in regions. Scale bars: 10 µm (main panels), 1 µm (insets).

(E) Pearson correlation coefficients for quantifying colocalization between PCM1 and client proteins. Fold change is calculated by comparing the mean value of serum starved cells to the mean of asynchronous cells. Results are from two biological replicates, n = 30 cells per condition. Statistical significance was determined using a t-test comparing treatment and control for each colocalization pair (ns > 0.05, **P < 0.01, ****P < 0.0001).

Figure 7

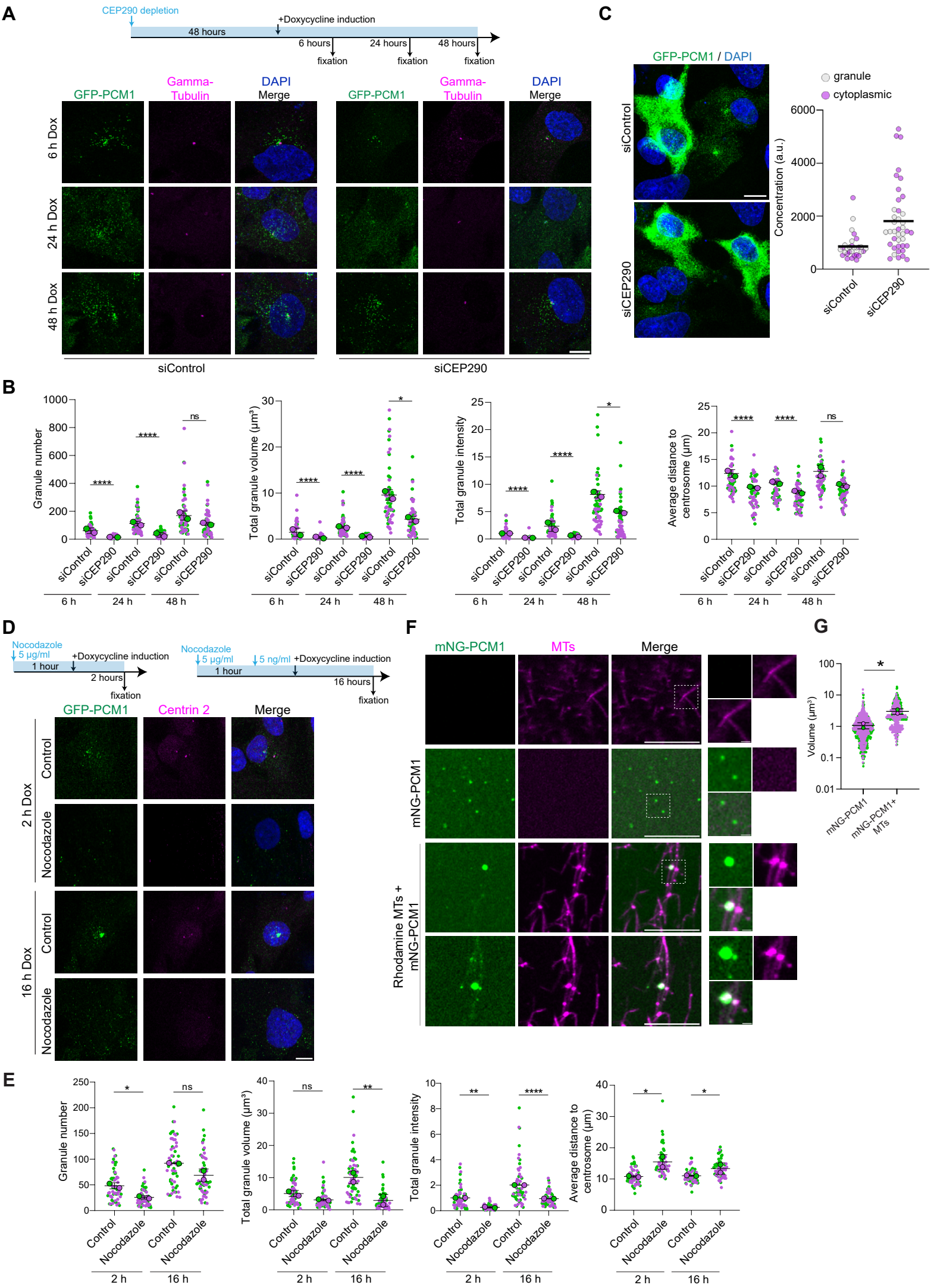
A
CEP290 depletion
+Doxycycline induction
48 hours
6 hours
24 hours
48 hours
fixation
GFP-PCM1
Gamma-Tubulin
DAPI
Merge
6 h Dox
24 h Dox
48 h Dox
siControl
siCEP290
C
GFP-PCM1 / DAPI
granule
cytoplasmic
Concentration (a.u.)
B
Granule number
Total granule volume (µm³)
Total granule intensity
Average distance to centrosome (µm)
6 h
24 h
48 h
D
Nocodazole
5 µg/ml
1 hour
2 hours
5 ng/ml
16 hours
Centrin 2
2 h Dox
16 h Dox
Control
Nocodazole
F
mNG-PCM1
MTs
Rhodamine MTs + mNG-PCM1
G
Volume (µm³)
mNG-PCM1+ MTs
E
2 h
16 h

Figure 7

Microtubules and clients modulate CS assembly.

(A) CEP290 promotes CS assembly. Representative confocal images of RPE1::PCM1 KO cells inducibly expressing GFP-PCM1 transfected with either siControl or siCEP290 before doxycycline induction. Cells were transfected with siRNAs for 48 hours, followed by induction for 6 hours, 24 hours or 48 hours. Cells were fixed and stained for anti-GFP (green), anti-gamma tubulin (cyan) and nucleus (blue). Scale bar: 10 µm

(B) Quantification of CS granule properties after CEP290 depletion from (A). Granule properties, including total volume of granules per cell (μm^3), average volume of granules per cell (μm^3), total granule intensity, granule number and average distance of granules to centrosome (µm) values were measured using Imaris software. Average values represent total values divided by the number of values for each cell. Average distance to centrosome values were quantified from the distance between granules and gamma-tubulin staining for each cell. Statistical significance was determined by the Student's *t*-test (paired and two-tailed). Results are from two biological replicates, green and magenta colored dots representing different replicates. n=30 cells cells per replicate. *:P<0.05; **:P<0.01, ***:P<0.001****:P<0.0001; ns: not significant.

(C) Effect of CEP290 depletion on the critical saturation concentration of PCM1. HeLa::PCM1 KO cells were transfected with either siControl or siCEP290. After 24 hours, the cells were transfected with a GFP-PCM1 construct. An additional 24 hours later, the cells were fixed and stained with an anti-GFP-Ab and DAPI to visualize DNA. Dark magenta circles indicate cytoplasmic localization of PCM1, while lighter magenta circles indicate granular localization. The critical concentration represents the mean value of granular concentration values observed. Results are from two biological replicates. Scale bar: 10 µm.

(D) Microtubules promote CS assembly. Representative confocal images of RPE1::PCM1 KO cells inducibly expressing GFP-PCM1 treated with nocodazole. Cells were either treated with 5 µg/ml nocodazole for 2 hours before 1 µM doxycycline induction for 2 hours or with 5 µg/ml nocodazole for 1 hour, then with 5 ng/ml nocodazole and 1 µM doxycycline for 16 hours. Results are from two biological replicates, n=30 cells per replicate. Cells were fixed and stained for anti-GFP (green), anti-centrin 2 (cyan) and DAPI for nucleus (blue). Scale bar: 2 µm.

(E) Quantification of CS granule properties after nocodazole treatment from (D). Granule properties, including total volume of granules per cell (μm^3), average volume of granules per cell (μm^3), total granule intensity, granule number and average distance of granules to centrosome (µm) values were measured using Imaris software. Statistical significance was determined by the Student's t-test (paired and

two-tailed). Results are from two biological replicates, green and magenta colored dots representing different replicates. n=30 cells cells per replicate. *:P<0.05, **: P<0.01, ***:P<0.001, ****:P<0.0001; ns: not significant.

(F) mNeonGreen-PCM1 and taxol-stabilized microtubules, polymerized from purified bovine tubulin and labeled with Alexa Fluor 568, were prepared in BRB80 buffer both individually and in combination. These were introduced into flow chambers and imaged. Scale bars: 10 μm (main panels), 1 μm (insets).

(G) Volume of mNeonGreen-PCM1 condensates plotted for each condition, with the y-axis on a log10 scale for the mNeonGreen-PCM1 only and the additive microtubules condition. Results are from two biological replicates, green and magenta colored dots representing different replicates.